Ballistic Electron Transport in GaAs/AlGaAs Mesoscopic Structures

by

Kazuhito Tsukagoshi

DISSERTATION IN PHYSICS

THE OSAKA UNIVERSITY

GRADUATE SCHOOL OF SCIENCE

TOYONAKA, OSAKA

Ballistic Electron Transport in GaAs/AlGaAs Mesoscopic Structures

by

Kazuhito Tsukagoshi

Dissertation in Physics

The Osaka University
Graduate School of Science

September, 1995

Acknowledgments

The author is grateful to Professor Kazuo Murase, who introduced the author to this field of research, for encouragement, for valuable suggestions, and for critical reading of the manuscript.

He is indebted to Dr. Sadao Takaoka for valuable discussions, for valuable advice in this research, and for critical reading of the manuscript.

He is grateful to Dr. T. Nagao for frequent and useful discussions, and for investigations by the calculation about the electron transport in the periodic potential.

He would like to thank Dr. K. Oto for experimental advices.

He is indebted to Dr. J. Takahara for instruction in the sample preparation and for stimulating and encouraging discussions.

He thanks Mr. F. Wakaya for discussions about fundamental properties in the GaAs/AlGaAs heterostructure.

He is indebted to Mr. S. Wakayama, Mr. M.Haraguchi, Mr S. G. Inoue, and Mr. K. Haruta for their help in the experiment and for useful discussions.

He would like to express his appreciation to Dr. T. Ohtsuki, Dr. K. Fujii, and Dr. T. Nakanishi for valuable discussions.

He also thanks Mr. H. Okada of Sumitomo Electric Industry Co.,Ltd. and Mr. K. Kasahara of NEC Corp. for providing high quality GaAs/AlGaAs heterostructures.

He is grateful to Prof. S. Namba and Prof. K.Gamo for providing facilities for microfabrication technology.

He is grateful to Prof. S. Hiyamizu, Dr. S. Shimomura, Dr. Y. Liu, Mr. T. Kishi, and Mr. M. Yamamoto for help in the observation of surface image of antidot sample by atomic force microscope.

He acknowledges the financial support from the Research Fellowships of the Japan Society for the Promotion of Science for Young Scientists. This work is partially supported by a Grant-in-Aid for Scientific Research on Priority Area from the Ministry of Education, Science and Culture.

The author thanks Prof. S.Ishida, Prof. S. Sugai, Dr. O. Matsuda, and all members of Murase Laboratory for their encouragements during this study.

Finally, he wishes to thank his parents and his wife Makiko Tsukagoshi for their constant encouragements.

Abstract

Ballistic electron transports in a submicron-sized mesoscopic structures made from the GaAs/AlGaAs two-dimensional electron gas (2DEG) are investigated. The electron transport in mesoscopic structure is influenced by the sample boundary and by a small amount of residual impurities in GaAs/AlGaAs heterostructure. In this thesis, we investigate I. magnetic electron focusing effect, II. electron emission distribution from an oblique wire, III. transport property in the lateral antidot lattice. The outlines of these experiments are shown as follows.

I. Study of Magnetic Electron Focusing Effect (Section 4.1)

The magnetic electron focusing effect has been investigated in a multi-terminal device. From decaying behavior of the magnetoresistance peaks owing to the focusing effect with several separation lengths between an electron emitter and a collector, we deduce the ballistic mean free path (l_b) which is considerably shorter than the conventional one (l_e) determined by the Hall measurement. The ratio of l_b to l_e is almost the same, and both mean free paths increase with increasing carrier density of 2DEG (n_s). The specularity of the sample boundary is determined by the damping ratio of the peak heights when the electrons are reflected at the sample boundary.

Furthermore, even in a configuration, where the focused electrons can enter into a extra probe which is located between the emitter and the collector probe, the focusing effect can be clearly observed. By the examinations of a new type of device with a byway which connects two extra probes through a 2DEG path, it is found that the "extra probe reflection" stems from the electrons re-emitted from the extra probe whose chemical potential is increased by the entering electrons.

II. Investigation of Electron Emission distribution from Oblique Wire (Section 4.2)

Electron stream emitted from a narrow wire to the wide 2DEG region distributes in forward directions. Electrons are collimated with decreasing width of the emitter which is gradually connected to 2DEG. By wheeling the electron stream in the magnetic field, we investigate the angular distribution of electrons from an oblique wire which is obliquely connected to wide 2DEG region. The average direction of electron stream from the oblique wire shifts from the wire direction. It is found that the electron angular distribution depends not merely on the wire direction but also on the structure just at the orifice of the wire.

III. Transport Property in Lateral Antidot Lattice (Section 4.3)

In lateral antidot superlattices, in which the potential modulated pillars (antidots) are regularly superimposed on 2DEG, the magnetoresistance shows characteristic peaks of the arrangement of antidots. Because the origin of peaks seem to be ascribed to the cyclotron motion with the encircling orbit around some antidots, the magnetoresistance has been called "commensurability oscillations".

In this description, we examine the behaviors of oscillations by changing the current flow direction with relation to the anisotropic lattices. Investigated anisotropic antidot lattices are the one-directionally disordered ones, several rectangular ones, and several isosceles triangular ones. The fluctuation of the antidot location generally suppresses the peaks of commensurability oscillations, although the fluctuation parallel to the current flow direction is not effective in the suppression of the peak. In several rectangular lattices, the peaks appear at the cyclotron diameters with the lattice spacing perpendicular to the current. Moreover, in several isosceles triangular lattices, the peak fields are determined by the nearest neighbor distance between the antidots. From the experimental results, we find that the commensurability oscillations in the high fields originate from the electrons on "runaway trajectory" in which the electrons skip away along the antidot array perpendicular to the current flow direction.

Contents

Chapter 1

Introduction

In a recent quarter of a century, a lot of novel quantum transport phenomena have been discovered in the solid mesoscopic systems: Mesoscopic structures are larger than the atomic scale system but smaller enough than the macroscopic system, which cannot be treated by the familiar statistical physics.[1-4] The mesoscopic systems can be obtained owing to the developments in lithographic technique fabricating the submicron structures accurately.[5] Below the liquid helium temperature (4.2 K), the phase coherent length of electrons is of the order of a few micron, and in very high quality semiconductors the mean free path exceeds decamicron. Thus, the transport properties in these systems are characterized by the specific structure in the sample owing to the order or the disorder of potential near the conduction channels of electrons.

Remarkable phenomena in the mesoscopic region and the related historical events are shown in Table 1.1. It is surprising that some effects in the table can be described accurately by the two physical constants: single electric charge "e" and Plank's constant "h", although the electrons transmit in the various kinds of structures. Some of important mesoscopic phenomena in Table 1.1 are introduced below.

- Al'tshuler–Aronov–Spivak (AAS) effect.[6,7]
  The conductivity of a small metal tube oscillates as a function of the magnetic flux threading through the tube with a period of $h/2e$.

- Universal conductance fluctuations.[8,9]
  In a narrow wire containing some potential disorders, its conductance fluctuates with magnetic fields in the amplitude of square root average by $2e^2/h$.

- Aharonov–Bohm (AB) effect.[10,11]
  Conductance through a ring structure oscillates with the period corresponding with h/e as the magnetic flux through the area encircled by the ring increases.

- Quantized conductance through a point contact.[12,13]
  Conductance through a narrow channel is quantized at the multiple of $2e^2/h$.

- Single electron tunneling.[14]
  Single electron tunnels a small dot structure sequentially.

Most of the origins in above phenomena can be understood by staring from the *Landauer Formula*, which relates the conductance to transmission probability.[1] Details of the *Landauer Formula* are introduced in the next chapter.

Moreover, in the mesoscopic structure, the boundary between the sample bulk region and the probe regions is indistinct and "non-locality" coming from the outside regions between the voltage probes becomes pronounced.

In this thesis, we focus on the ballistic electron transports in mesoscopic structures made from GaAs/AlGaAs two-dimensional electron system. By utilizing the magnetic electron focusing effect, we investigate the scattering mechanisms in the 2DEG and at the sample boundary. We also investigate nonlocal effect by the extra probes. (Chapter 4.1) The angular distribution of electrons emitted from a narrow wire is examined. (Chapter 4.2) We investigate the electron transport properties in the antidot lattice by studying the influence of the anisotropy, the disorder effect of antidot location. From the relation between commensurability oscillations and current flow direction, we find the origin of the commensurability oscillations. (chapter 4.3)

Table 1.1: Recent topics in mesoscopic physics and the related historical events. In the table, "Ex" shows experiment and "Th" theory.

year	
1931 Th	Reciprocal relations in irreversible process (L.Onsager)[15]
1945 Th	Onsager's principle of microscopic reversibility (H.B.G.Casimir)[16]
1956 Th	Fermi Liquid Theory (L.Landau)[17]
1957 Th	Kubo formula (R.Kubo)[18]
Th	Landauer formula (R.Landauer)[1]
1958 Th	Anderson localization (P.W.Anderson)[19]
1959 Th	Aharonov-Borm effect (Y.Aharonov and D.Borm)[10]
1965 Th	Electron focusing effect (Yu.V.Sharvin)[20]
1970 Th	Semiconductor superlattice (L.Esaki and R.Tsu)[21]
1974 Ex	Electron focusing effect in Bi-crystal (V.S.Tsoi)[22]
1978 Ex	Modulation doping (R.Dingle *et al.*)[23]
1979 Th	Scaling theory (E.Abrahams *et al.*)[24]
1980 Ex	HEMT (T.Mimura *et al.*)[25]
Ex	Integer quantum Hall effect (K.von Klitzing *et al.*)[26]
1981 Th	AAS effect (Al'tshuler *et al.*)[6]
Ex	AAS effect in Mg tube (D.Yu.Shervin and Yu.V.Shervin)[7]
1982 Ex	Fractional quantum Hall effect (D.C.Tsui *et al.*)[27]
1983 Th	Fractional quantum Hall effect (R.B.Laughlin)[28]
1984 Ex	UCF in Au-Pb wire (C.P.Umback *et al.*)[8]
1985 Th	UCF theory (A.D.Stone)[9]
Ex	AB effect in Au ring (R.A.Webb *et al.*)[11]
1986 Th	Landauer-Büttiker formula (M.Büttiker)[3]
1988 Ex	Quantized conductance through a point contact (B.J.van Wees *et al.*, D.A.Wharam *et al.*)[12,13]
Ex	Quenching of Hall effect (M.L.Roukes *et al.*)[29]
Ex	Bend resistance (Y.Takagaki *et al.*)[30]
1989 Th	Composite Fermion (J.K.Jain)[31]
Ex	Composite Fermion (H.W.Jiang *et al.*,R.L.Willet *et al.*)[32,33]
Ex	Commensurability oscillations in washboard potential (D.Weiss *et al.*)[34]
Ex	Commensurability oscillations in antidot potential (E.S.Alves *et al.*)[35]
Ex	Single electron tunneling (U.Meirav *et al.*)[14]
1992 Ex	Quantum chaos in stadium structure (C.M.Marcus *et al.*)[36]

Chapter 2

Review of Transport Properties in Mesoscopic Systems

2.1 Introduction

In the classical approach, the current through the system is proportional to the average of electron velocities which are determined by the time between collisions with scatterers. Thus, the resistances of any piece of a system may be predicted. The resistance is calculated usually by the Boltzmann approach.[37] In the mesoscopic system, however, the velocity averaging approach breaks down, because the electron mean free path or coherent length are comparable to the system size and the number of scatterers vary in piece of a system. This means that "an electron stream" in a piece of system much differs from the average current which flows through the whole system. Furthermore, electron trajectories are also influenced by the fine structure of the system boundary. Thus, we must treat the conductance of the system as a result of the propagation of the electron wave and the wave interference. This conductance can be described by the *Kubo formula* and the *Landauer formula.*

The standard framework for the description of the conductivity is given by the *Kubo formula*, which describes the linear response to an electromagnetic potential. This formula is more convenient for analytic calculation. It is suitable for relatively wide system, *e.g.*, periodic potential system, to apply this formula. On the other hand, it is good approach for the *Landauer formula* and the *Landauer-Büttiker formula* to treat the mesoscopic system with multi-probe or with the effective boundary, because these systems can be determined by the electron transmission probabilities from one probe to another probe. It is proved that the *Kubo formula* and the *Landauer-Büttiker formula* are equivalent and complement each other.[38,39]

In this chapter, we introduce the *Kubo formula* and the *Landauer formula* as a review for the transport properties in the mesoscopic system.

2.1.1 Kubo formula

The external field is treated as a small perturbation on the equilibrium state of many particle systems, eliciting a *linear response*, whose magnitude measures the corresponding transport coefficient. The electrical conductivity tensor may be expressed absolutely by the *Kubo Formula*[18]:

$$\sigma_{ij} = \frac{1}{k_B T} \int_0^\infty \langle \tilde{j}_i(t) \tilde{j}_j(0) \rangle \, dt \quad , \quad (i, j = x, y, z) \quad . \tag{2.1}$$

In other words the conductivity depends on the *time correlation* between a component of the current operator $\tilde{j}_j(0)$ at zero and the component $\tilde{j}_i(t)$ at the some later time t, integrated over all time and evaluated as the average of the expectation value of the product over the equilibrium ensemble. The average value of $\tilde{j}$ is zero, but the decay of *fluctuations* in the current precisely depends on the features of the impurity scattering which would govern the response to an external field.

2.1.2 Landauer formula

The *Landauer formula* has been originally derived for a strictly single channel conductance.[1] To derive this conductance, we consider the steady state of electrons among the sample and the various chemical potential in the leads (Fig. 2.1(a)). In the assumption of ideal leads, the scatterings of the electrons due to the random potentials occur only in the sample and the inelastic collisions occur mainly in the contact pads outside the sample. When the small chemical potential difference (μ_L, μ_R) is applied to two current probes, the conductance (G), defined as the current flow level by the voltage drop (V), is proportional to the transmission coefficient of the sample (T). Under the voltage drop ($V = \mu_L - \mu_R$), the number of electrons (Δn) approaching the sample from the left side in one dimension

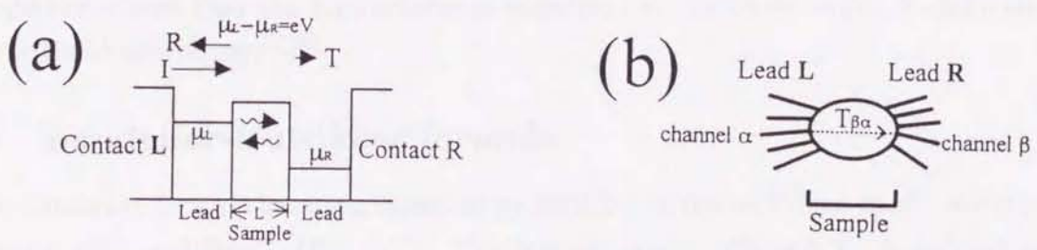

Figure 2.1: (a) Geometry in the considerations for the *Landauer formula*. (b) A model for transmitting electron through the sample. There are some channels in leads and the electron transmits from channel α in lead L to channel β in lead R through the sample with transmission probability $T_{\beta\alpha}$.

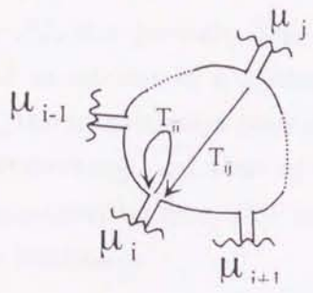

Figure 2.2: Sample with multilead. An electron from lead j transmits to lead i with the probability T_{ij}. T_{ii} represents a reflection probability in lead i.

$(\partial n/\partial E = 2/hv)$ in an unit time is

$$\Delta n = 2 \times \frac{1}{2} \times \frac{eV}{(\frac{hv_F}{2})} \times v_F = 2eV/h \quad , \tag{2.2}$$

where up and down spins are considered. Since only $T\Delta n$ electrons can transmit the sample, the current flow level I is given by $I = eT\Delta n = (2e^2/h)TV$. Thus, the conductance is determined by

$$G = I/V = (2e^2/h)T \quad . \tag{2.3}$$

The measured resistance is proportional to $1/T$. If there are some channels in leads and the electron transmits from channel α in lead L to channel β in lead R with transmission probability $T_{\beta\alpha}$ (Fig. 2.1(b)), this equation is written as

$$G = I/V = (2e^2/h)\sum_{\alpha,\beta} T_{\beta\alpha} \quad . \tag{2.4}$$

When the scattering in the sample is rare, transmission probability $T_{\beta\alpha}$ is $T_{\beta\alpha} \sim \delta_{\beta\alpha}$. If N-channels exist below the Fermi energy, the conductance is

$$G = I/V = (2e^2/h)N \quad . \tag{2.5}$$

This equation shows that the conductance is quantized at $(2e^2/h)N$ under N-channels conductor without scattering.[12,13)]

2.1.3 Landauer-Büttikker formula

The *Landauer formula* has been extended by Büttiker to the multilead case.[3)] We consider a scatterer with multilead. (Fig. 2.2). The transmission coefficient T_{ij} is defined as the probability that the electron transmits from lead j to lead i. When the electrons approaching a sample region from one lead j transfer to the other lead i, total current I entering in to lead i is given by

$$I_i = (2e/h)\left[N_i\mu_i - \sum_{j\neq i} T_{ij}\mu_j\right] \quad , \tag{2.6}$$

where N_i is the channel number below the Fermi energy in lead i. This equation is known as the *Landauer-Büttiker formula.* This formula is advantageous for conceptual understanding and numerical calculation in a scatterer with multilead.

Moreover, the transmission probability is correlated with the magnetic field (B). Owing to current conservation and time-reversal invariance, transmission probability is $T_{ij}(B) = T_{ji}(-B)$. Consequently, from this magnetic reversal relation, the measured magnetoresistance has the relation

$$R_{ij,kl}(B) = R_{kl,ij}(-B) \quad , \tag{2.7}$$

where $R_{ij,kl}$ shows a four-terminal measurement configuration ($R_{ij,kl} = (\mu_k - \mu_l)/(eI_{i\rightarrow j})$). This result also satisfies the *Onsager-Casimir symmetry relations.*

Chapter 3

Experimantal procedure

3.1 Introduction

Owing to the development of the epitaxial growth of the crystal by the molecular beam epitaxy (MBE)[40] and the modulation doping technique,[23] the mean free path of electrons in the semiconductor has been remarkably enhanced. Recently, in GaAs/$Al_xGa_{1-x}As$ (=GaAs/AlGaAs) heterostructure obtained by MBE, the electron mobility well exceeds 10^6 $cm^{-2}/Vsec$.[41-43] Moreover, owing to the recent remarkable progress of the fabrication technique,[5] we can make a mesoscopic-sized sample readily. In this study, a high-quality crystal, the micro-fabrication and the low temperature measurement are necessary. In this chapter, details of the experimental procedure are introduced.

3.2 Sample preparation

3.2.1 GaAs/AlGaAs heterostructure

Our devices with a mesoscopic size were made from a modulation doped GaAs/AlGaAs heterostructure so-called "HEMT (High Electron Mobility Transistor)".[25,41,44] Figure. 3.1(a) shows a typical layer diagram with a single-hetero junction providing 2DEG which consists of the following layers; 600 nm of GaAs followed by 15 nm of undoped AlGaAs spacer, then 40 nm AlGaAs doped by 2×10^{18} cm^{-3}-Si and finally a 5 nm AlGaAs cap. The fundamental structures used in this thesis are similar ones but each layer thickness is changed slightly. The conduction band profile is shown in Fig. 3.1(b). The energy difference between the bottom of the conduction band of AlGaAs and GaAs allows the electrons to fall into the GaAs from the donors in the AlGaAs. Because the electrons are separated from the ionized donors, the mobility of the electrons is much higher than that of a bulk GaAs. Moreover, the mobility is enhanced by the AlGaAs spacer inserted between the electrons and the ionized donors, whereas the carrier density decreases.[41,45-47] The electrons are confined strongly near the spacer layer by the "space charges" which are ionized donors in Si-doped AlGaAs layer, and are quantized in the confined potential. When the Fermi energy

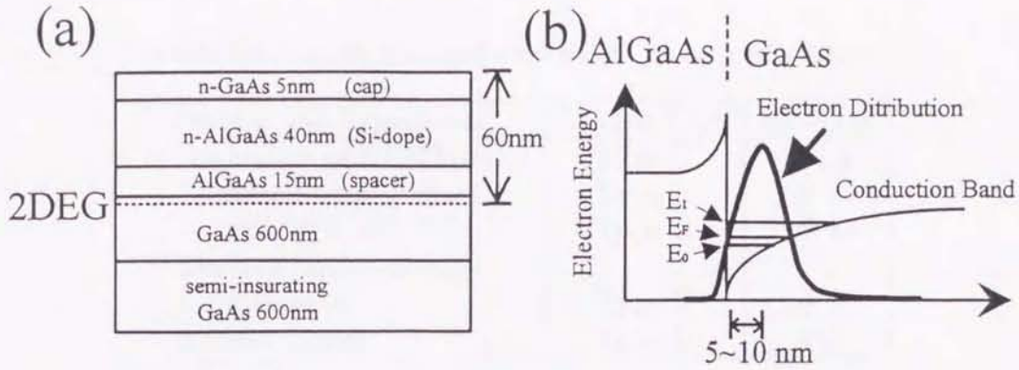

Figure 3.1: (a) Typical layer diagrams of GaAs/$Al_xGa_{1-x}As$ heterostructure (HEMT# 2). The ratio of x is 0.265. In another wafer, each layer width is varied slightly whereas the layer order is not changed. The substrate is (311)A-orientated GaAs crystal. (b) Conduction band diagram in GaAs/AlGaAs heterostructure.

Table 3.1: Electronic characteristics of the heterostructures. Carrier density (n_s), mobility (μ) and mean free path (l_e) are appraised by Hall measurement in Type C sample.

HEMT-No.	dark			illumination		
	n_s $10^{11}/cm^2$	μ $cm^2/Vsec$	l_e μm	n_s $10^{11}/cm^2$	μ $cm^2/Vsec$	l_e μm
1	3.2	140	13	4.1	186	20
2	3.8	57	5.8	5.2	104	12

determined by the carrier density is below the bottom of second subband level, the electrons occupying the conduction band form a two-dimensional electron gas (2DEG).

Moreover, the mobility of 2DEG grows by decreasing phonon scatterings.[41,47,48] Electron mobility of our heterostructure exceeds 10^6 cm^2/Vs at low temperatures. The electronic characteristics of the heterostructure are shown in Table 3.1. These values are derived from the Hall effect measurement and the zero-field resistance at 1.5 K. Carrier density of 2DEG is controlled by the illumination from the light emitting GaAs diode (LED: wave length = 950 nm). When the illumination supplies the extra conduction electrons from DX-centers in the Si-doped layer, the atomic configuration around each donor atom changes, because the charge state of the DX level is changed.[49] At low temperatures where kT is smaller than an activation energy for the capture of an electron from the conduction band to the DX-center, electrons conduct persistently. Thus, the carrier density do not change for a long time after putting out the light. This effect is known as "persistent photoconductivity (PPC) effect". Consequently, the carrier density in 2DEG increases by illumination.

The used HEMT in each experiment and the sample type are shown in Table. 3.2.

Table 3.2: Sample type and used HEMT in each experiment.

Section and Experiment	Sample Type	HEMT#
Evaluation of HEMT wafer	Type C	# 1,2
Electron focusing effect	Type A	# 1
with byway	Type B	# 2
Electron emission angle		
with gate	Type E	# 2
Antidot lattice	Type D	# 2

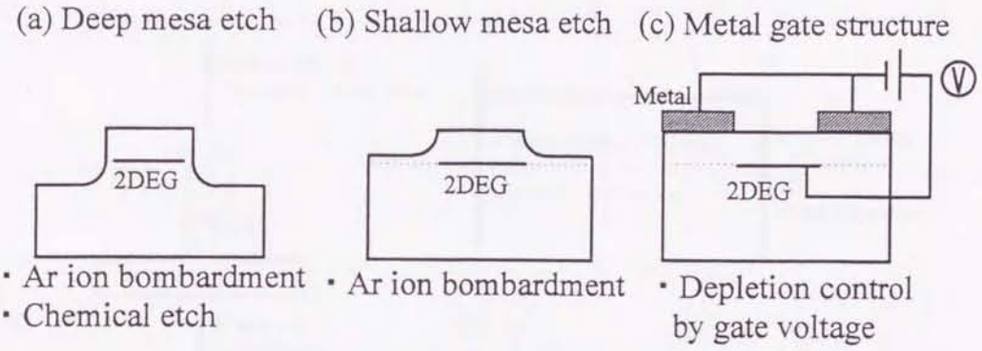

Figure 3.2: Typical mesoscopic structures fabricated by different techniques. (a)Deep mesa structure by Ar ion etching or chemical etching, (b) shallow mesa structure by Ar ion bombardment, and (c) gate-controllable structure by applying suitable negative voltage to the metal for depleting the electron beneath the gate.

3.2.2 Fabrication of mesoscopic structure

Typical sample structures are shown in Fig. 3.2. A deep mesa structure by chemical etching (Fig. 3.2(a)) has little damage in its fabrication, but is not suitable for the fabrication of the structure smaller than 1 μm size. So, it is used for appraising the electric characteristics of the wafers. By using conventional electron beam (EB) lithography and Ar ion bombardment, we can make the fine structure with sub-micron size (Fig. 3.2(b)). The 2DEG region irradiated by Ar ions is depleted. Because only surface of the heterostructure is etched to avoid the unnecessary damage in the sample by Ar ion bombardment, this technique is called "shallow etching". Gate structures are made by the EB lithography, metal deposition, and lift off technique (Fig. 3.2(c)). Gate structure is transferred by applying suitable negative voltage to metal gate for depleting the electron beneath it, and can control the wire width satisfactorily.

General fabrication process consists of the etching of crystal, the construction of metal gates, and the make of ohmic contacts. Figure 3.3 shows a flow chart for making various type of samples (Type A−E). Samples could be made by the combinations from mesoscopic

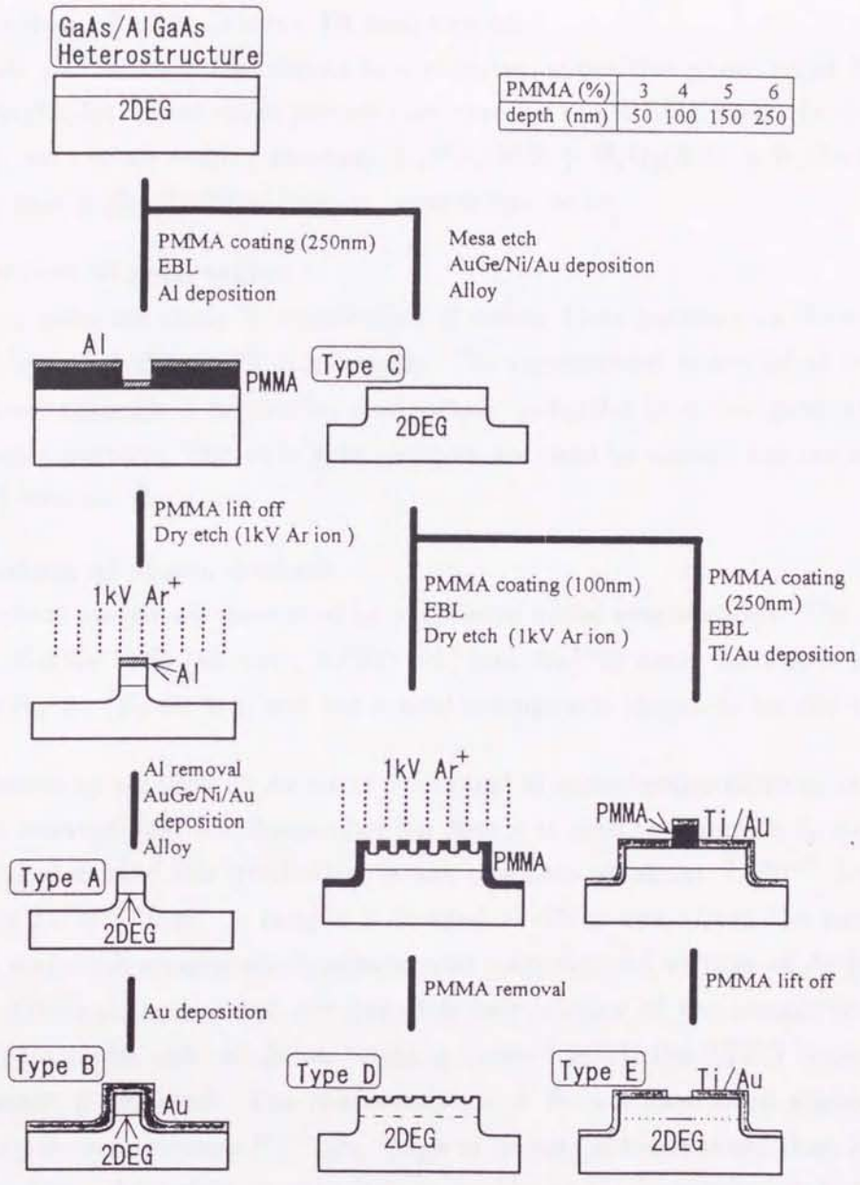

Figure 3.3: A flow chart for sample fabrication.

region, wide region, gate region and ohmic contact.

1. **Fabrication of mesoscopic (submicron) region**

   The pattern with submicron region is drawn by using EB lithography on the PMMA (=PolyMetylMethacrylate: weight-average molecular weight$\sim 9\times10^5$) resist coated on the heterostructure. After evaporating thin Al film on it and lifting the resist off, the patterns are transferred to the heterostructure by 1 kV accelerated Ar ion. The etching rate is about 4nm/min. In other case, the trench patterns on the resist are directly transferred to heterostructure by Ar ion bombardment. This technique is known as "trench etching".[5)]

2. **Fabrication of wide (above 10 μm) region**

   The wide patterns are transferred to a negative or positive photo-resist film by using UV lithography. Those resist patterns are used for the etching mask. In the case of wet etching, we use an etching solution (H_2PO_4(85%): H_2O_2(30%): H_2O=1:1:30). The etching rate is about 100nm/min at room temperature.

3. **Fabrication of gate region**

   Schottky gates are made by evaporation of metal. Gate patterns on the resist are also formed by using EB or UV lithography. The confinement potential at the boundary of electron channels is formed by electrostatic potential from the gates in the case of mesoscopic pattern. The wide gate patterns are used to control the carrier density of channel beneath the gates.

4. **Fabrication of ohmic contact**

   The contact metals are deposited by successive metal evaporations. The metal layers are Au/Ge(Ge-12%: 100 nm), Ni(300 nm) and Au(500 nm). Anneal is performed in flowing H_2/Ar (H_2-80 %), and the anneal condition is chosen to be 350°C for 4 min.

Bombardment by accelerated Ar ion is performed at room temperature in an dry etching apparatus. A conventional Kauffman-type ion source is used to generate Ar ions. Pure-Ar gas is introduced during the irradiation in the chamber at about 7×10^{-5} Torr after the evacuation by 2×10^{-5} Torr. A sample is located at 25cm away from the ion source and is rotated to avoid inhomogeneous bombardment. Accelerated voltage of Ar ion is chosen to be 1 kV. Although accelerated Ar ions etch only surface of the sample at the rate of about 4 nm/min under this condition (etching time$\sim$3 min), the 2DEG region irradiated by the ion beam is depleted. The characteristics of Ar ion have been studied in detail. Following previous experiments,[50-52] the range of defects extends more than 100 nm from the sample surface. According to calculations by Monte Carlo simulation techniques, the projected ranges of Ar at 1 kV are about 2.5 nm.[53-56] The discrepancy of more than an order of magnitude may be explained by mechanisms such as channeling along the suitable crystal direction,[57] enhanced diffusion of implanted species by ion bombardment, and rapid propagation of defects such as vacancies, Frenkel pairs, and dislocations.

3.2.3 Measurement system

After Pt-wires are connected to the metal pads of sample contacts through conductive silver paint, the sample is mounted on the holder in the cryostat and electric leads are derived out. Whole measurement system is shown in Fig. 3.4. The magnetoresistance up to 13kG is measured at the temperature below 4.2 K. The temperature below 4.2 K is obtained by pumping ^{4}He gas out, or by pumping ^{3}He gas out from the sample room through ^{3}He

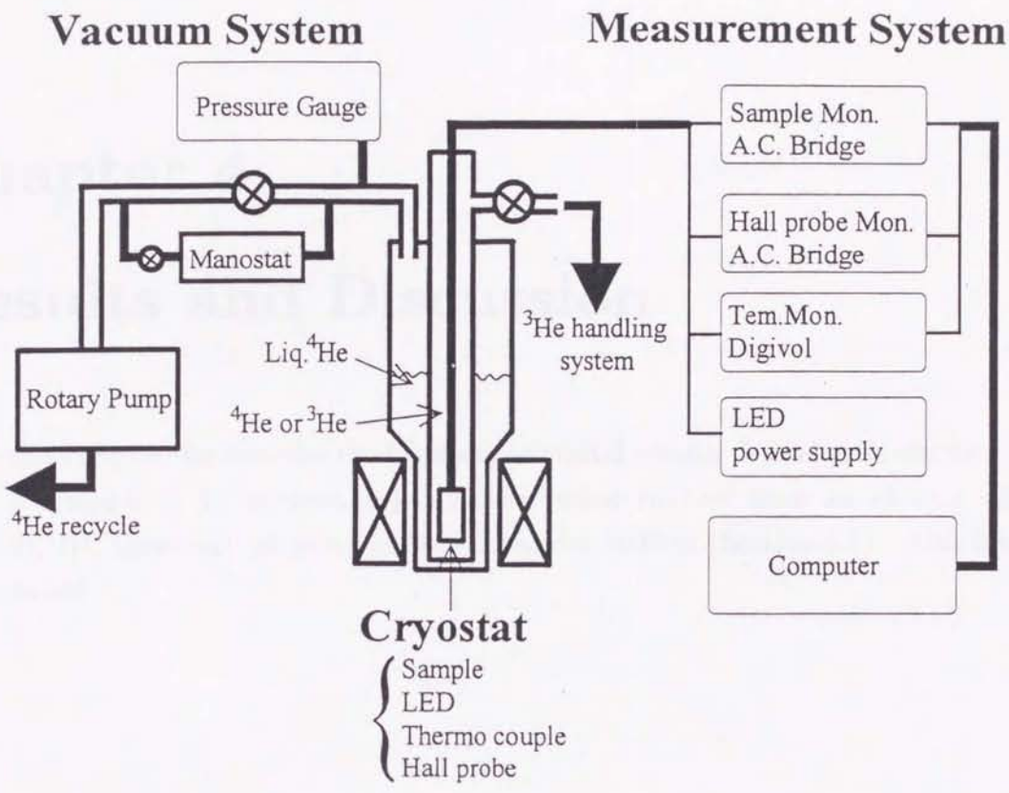

Figure 3.4: Measurement system for transport properties in mesoscopic GaAs/AlGaAs device.

handling system.

The measurement is made by using a four-terminal resistance method: Two of these contacts are used to supply and draw current from the sample, and the potential difference is measured between another pair of probes. Resistance is measured by an ac resistance bridge (RV Electroniikka AVS-46) operated at 15 Hz. The magnetic field in the sample is monitored by the Hall probe in the back side of the sample. A light emitting diode (LED) is set near the sample to control the sample carrier density. Data of the magnetoresistance are taken into a computer and are stored.

Chapter 4

Results and Discussion

In this chapter, we describe the three experimental results: I. Magnetic electron focusing effect (Section.4.1), II. electron angular distribution emitted from an oblique wire (Section.4.2), III. transport property in lateral antidot lattices (Section.4.3). Also discussions are included.

4.1 Magnetic Electron Focusing Effect

4.1.1 Introduction

The electrons in the 2DEG at low temperatures can go straight for more than the scale of microns until those are scattered by residual impurities.[47,42,43] In such 2DEG, the transport properties show the curious and interesting electron propagation phenomena. An electron focusing effect is one of them. The electrons emitted from a narrow wire to a wide 2DEG have a peculiar angular distribution. The electron distribution becomes wider as electrons go away from the orifice of the wire. (This problem is discussed in next chapter.) The emitted electrons can be "focused" by the "electrostatic lens"[58-60] or by the "magnetostatic lens"[20,22,60-75] (Fig. 4.1). In the case of the electrostatic lens (Fig. 4.1(a)), emitted electrons are focused by a spatial modulation of electrostatic potential along the electron trajectories (Fig. 4.1(a-2)) in analogy with modulation of the dielectric constant in conventional light-wave optics. Spector *et al.* and Sivan *et al.* have succeeded in controlling ballistic carriers via electrostatic gates which can act as refractive elements for the electron path. Spector *et al.*

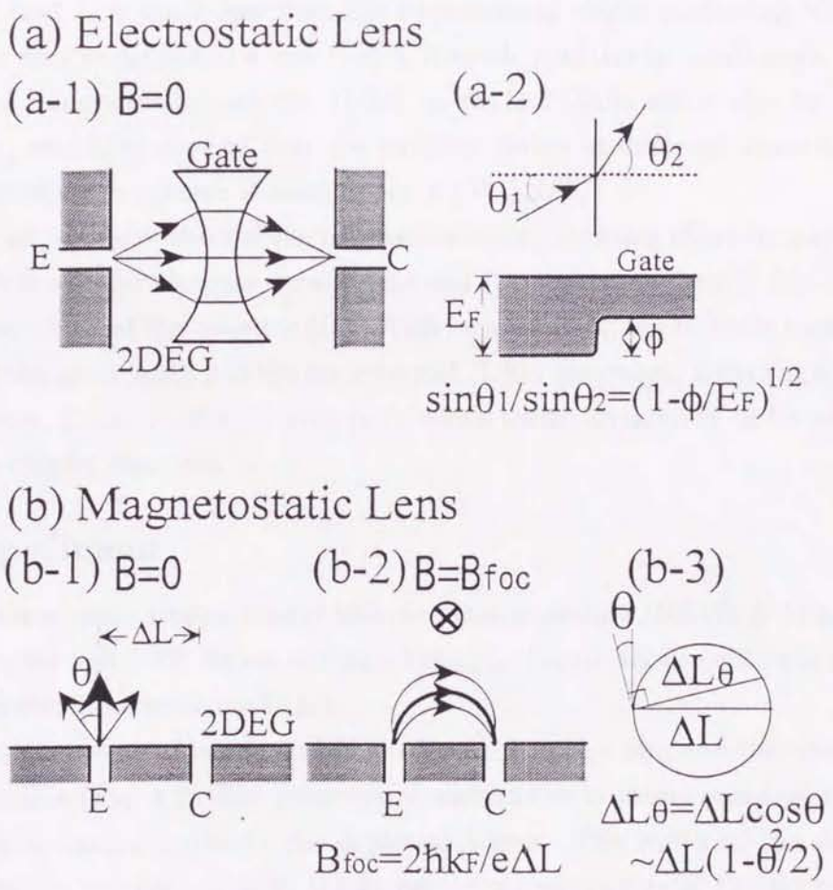

Figure 4.1: Schematic view of mechanism of electron focusing effect. (a)Electrostatic focusing effect and (b)magnetostatic focusing effect.

also have made an electrostatic "prism" by using the same technique,[60,76] and have showed its usage to switch the path of electrons among several collectors. On the other hand, in the case of magnetic field lens (Fig. 4.1(b)), the electron trajectories in the magnetic field ($B = B_{\rm foc}$) reach the collector when the cyclotron diameters approach a separation between the emitter and the collector (ΔL). At $B = B_{\rm foc}$, emitted electrons (spreding angle=θ) finally focus on the collector (Fig. 4.1(b-2,b-3)), because the distance between the emitter and the electron reaching points (ΔL_θ) changes within the second order of θ ($\Delta L_\theta = \Delta L \cos\theta \sim \Delta L(1-\theta^2/2)$). This "self-gathering effect" are called "magnetic electron focusing effect". The magnetic field $B_{\rm foc}$ is $2\hbar k_F/e\Delta L$, where k_F is the Fermi wave vector.

The magnetic electron focusing effect has been first developed by Sharvin in 1965[20] and has been used to explore the Fermi surface of several pure metals and semimetals.[22,61,62] Most of these experiments show the very high specular reflection coefficient (specularity : p) of electrons at the sample boundary, where a surface roughness is the scale of the Fermi wavelength of the conduction electrons. Beenakker and van Houten *et al.* have observed this effect in high mobility GaAs/AlGaAs heterostructure with point contact gates.[63-65] Using similar technique, Spector *et al.* have evaluated a ballistic elastic scattering length ($l_{\rm b}$), and have revealed that $l_{\rm b}$ is much less than the conventional elastic scattering length ($l_{\rm e}$), and have explained this reduction in a way that $l_{\rm b}$ is much sensitive to small angle scattering.[66] Churchill *et al.* have investigated the 2DEG on (311)B GaAs substrates by the magnetic focusing effect, and have showed that the mobility defers in different directions in (311)B because the interface roughness is anisotropic in (311)B.[68]

In this report, we have studied the magnetic electron focusing effect by paying attention to the dependence of the electron density ($n_{\rm s}$) and the separation length (ΔL) between the electron emitter (E) and the collector (C). With increasing $n_{\rm s}$, the ballistic mean free path $l_{\rm b}$ increases, and the specularity p at the boundary of 2DEG decreases. Even the extra electrode is placed between E and C, the focusing peak which seems apparently to be reflected at the extra probe is clearly observed.

4.1.2 Experiment

Our device was made from a GaAs/AlGaAs heterostructure (HEMT# 1) and fabricated by EB-lithography and 1 kV Ar ion milling (Type A). Figure 4.2 presents the sample image by scanning electron microscope (SEM).

The intervals between adjacent probes are 8 μm : 2 μm : 4 μm, and the up-side is mirror image of down-side (Fig. 4.2. The geometrical width of each probe is about 1 μm, but the effective width is narrower due to the depletion layers. The width of the device is wide enough (20 μm) in comparison with the largest cyclotron radius of the magnetic electron focusing effect for the maximum E-C distance (ΔL=14 μm). The magnetoresistance was measured at 1.5 K by using a resistance-bridge operating at 300 nA AC current at 30 Hz. The

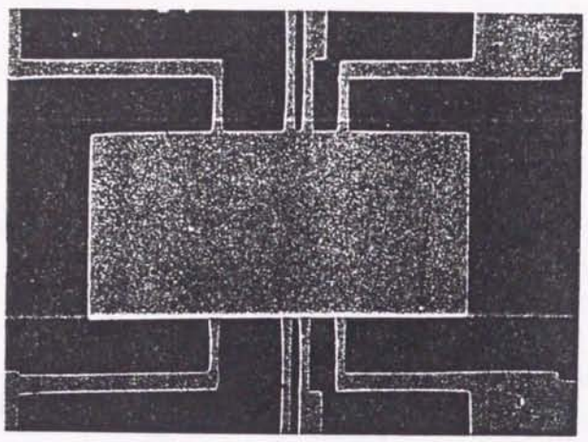

Figure 4.2: Image of sample surface by SEM. The interval between the adjacent probes in down-side is 8 μm : 2 μm : 4 μm, and the up-side is mirror image of down-side.

measurement was made by using a four-terminal measurement method. The nominal current flowed straightly from an upper to a symmetrically placed lower probe, and the voltage was measured parallel to the current path (inset of Fig 4.3). The negative current probe ($I-$) is the electron emitter and the negative voltage probe ($V-$) is the collector. When the electron emitted from the emitter is focused into the collector by the magnetic fields, the resistance peaks are observed. In this electrode configuration, the magnetic electron focusing effect is symmetric between positive and negative magnetic fields because of the symmetry of the device.

4.1.3 Results and discussion

4.1.3.1 Ballistic elastic scattering length estimated from electron focusing effect

Figure 4.3 shows the focusing effect for six different ΔL from $2-14$ μm at $n_s = 4.1 \times 10^{11}$ cm^{-2}. The fundamental focusing peak appears near zero-magnetic field where the cyclotron diameter accords with ΔL. The other peaks appear via the reflection at the sample boundary. The magnetic fields ($B_{\rm ref}$) of these peaks are integer multiples of $B_{\rm foc}$ ($B_{\rm ref} = B_{\rm foc} \times M$: where $M-1$ is the number of the reflection). The oscillations in higher magnetic fields ($\mid B \mid > 3$ kG) are the Shubnikov-de Haas (SdH) oscillations.

The negative resistance between the focusing peaks is also explained by the classical view as follows. When the condition of the focusing effect is not satisfied, that is, the electron is not focused into the collector, the electrons emitted from E pass the collector probe. These electrons are diffusively scattered until reaching the other voltage probe ($V+$ probe), and a part of them enter into $V+$ prove at all times. Thus, the voltage difference between two voltage probes becomes negative. As the separation ΔL increases, the passing electrons decrease and the negative resistance becomes smaller.

In Fig. 4.4(a), the amplitude of the peak-to-valley of the focusing effect is plotted v.s. ΔL on semi-logarithms. As ΔL becomes larger, the scattering probability of the electron increases, and the amplitude of the peaks decreases. If the decay of the amplitude would

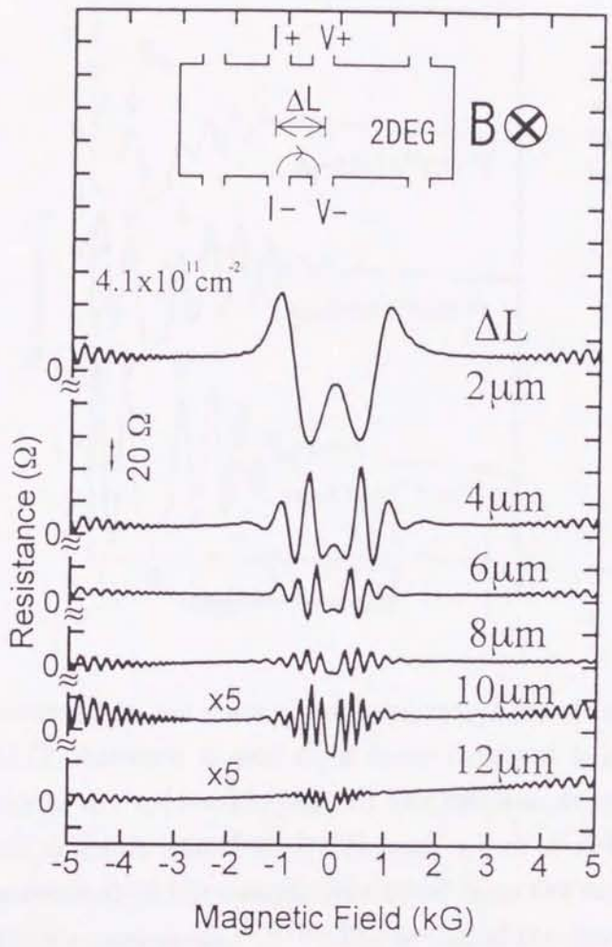

Figure 4.3: Magnetoresistances for various ΔL at $n_s = 4.1 \times 10^{11}$ cm^{-2}. The oscillations in higher magnetic fields ($|\ B\ | > 3$ kG) are the SdH oscillations. Inset shows a schematic view of device with multiprobe. Separation length ΔL varies from 2 μm to 14 μm by changing combinations of current and voltage probes.

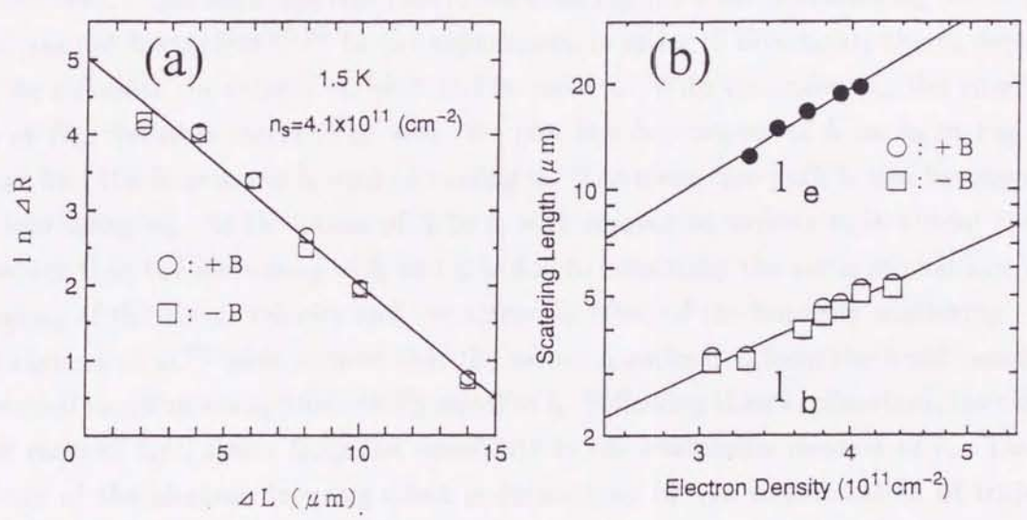

Figure 4.4: (a) Peak amplitude of magnetic focusing effect is plotted with respect to the emitter-collector separation length (ΔL). Line is a least square fit to $exp(-\pi\Delta L/2l_b)$ form with l_b=5.2 μm. (b) Electron density dependence of ballistic scattering length l_b and conventional elastic scattering length (l_e).

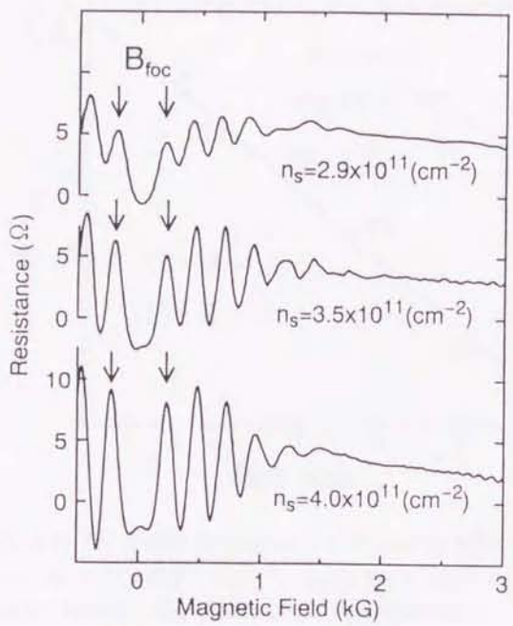

Figure 4.5: Magnetoresistances of ΔL=8 μm with different electron density (n_s). Amplitude of focusing effect becomes larger with increasing n_s.

be assumed to decrease as an exponential function of the electron trajectory path length ($\pi\Delta L/2$) between E and C, a decay constant l_b is defined, so that the amplitude is proportional to $exp(-\pi\Delta L/2l_b)$. At this electron density (4.1×10^{11} cm^{-2}), l_b is 5.2 μm. This length is much less than l_e (20 μm), which is determined by the conventional resistivity measurement of the sample fabricated from the same wafer. The trends are similar to the previous experiments.[66, 67, 70] The reason of the shorter l_b than l_e is that l_b is sensitive to the small angle scattering. The damage of the micro-fabrication may also reduce l_b.

Until now, it has been reported that l_b increases rapidly with increasing n_s, but this mechanism has not been clear.[67, 70] In our experiment, in order to investigate the n_s dependence of l_b, we irradiate the sample by LED and increase n_s. With increasing n_s, the amplitude of peak at B_{foc} becomes larger (Fig. 4.5). We plot the dependence of l_b on n_s in Fig. 4.4(b). We can find the increase of l_b with increasing n_s. The mean free path l_e also becomes longer with increasing n_s. As the ratios of l_b to l_e with respect to various n_s is almost the same, we deduce that the increasing of l_b and l_e is due to essentially the same mechanism, such as increasing of the Fermi velocity and the screening effect of the impurity scattering.

Hirayama *et al.*[77] have showed that the values l_b estimated from the bend resistance at the crossed junction are approximately equal to l_e. Following their explanation, the difference in the ratio of l_b/l_e stems from the sensitivity in the evaluation method of l_b. The signal intensity of the electron focusing effect is determined by the concentration of trajectories at the collector as shown in Fig. 4.1(b-2). In addition, when emitter-collector separation is varied, it is difficult for the electron focusing method to correctly treat the electron spreading effect because the number of small angle scattering may vary at the trajectories with the different curvature, and the ratio of the collector width to the separation between E and C

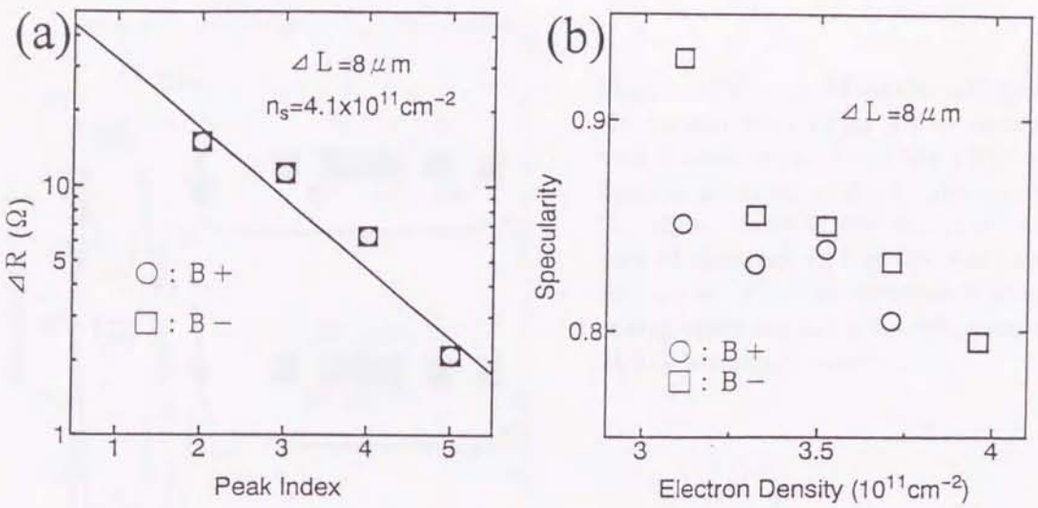

Figure 4.6: (a) Peak amplitude of focusing effect of ΔL=8 μm via reflection at the sample boundary with $n_s = 4.1 \times 10^{11}$ cm^{-2}. Line is a least square fit of p^M form with specularity $p \sim 0.8$. (b) Electron density dependence of specularity p.

changes too. Consequently, although further studies are necessary for l_b evaluation from the electron focusing effect with consideration of above points, l_b is closely related to l_e.

4.1.3.2 Specular reflection at the 2DEG boundary

The focusing peaks via the reflection at the 2DEG edge are reduced by the diffused reflection (Fig. 4.3). The specularity p is defined by the ratio of the intensity of the peak M to $M+1$. We deduce $p \sim 0.8$ from the slope of Fig. 4.6(a) of the signal of ΔL=8 μm. It have been reported that p relates with the fabrication method.[69,70,73,74] Figure. 4.6(b) shows the dependence of p on n_s. With increasing n_s, p decreases. Since the increasing of the electron density makes the width of the depletion layer at the sample boundary thinner and the effect of roughness introduced by the fabrication becomes more bare, the electron is more diffusively scattered. This n_s dependence agrees with the result by Wakaya et al.[73] Their experiment shows that p increases with increasing width of depletion layer which is controllable by the side-gates voltage. In addition to this depletion layer effect, the Fermi wavelength is reduced due to increasing of n_s. When the wavelength is comparable with the roughness, the electron with shorter wavelength tends to be scattered more diffusively than the one with the longer wavelength. If this effect is dominant, the order of the boundary roughness may be the order of the Fermi wavelength (~30 nm).

4.1.3.3 Reflection by the extra probe

In the cases of ΔL=6 μm, 10 μm, and 14 μm, the extra probes, which are not related to the voltage measurement, exist in the E-C separation. When the electrons from emitter can

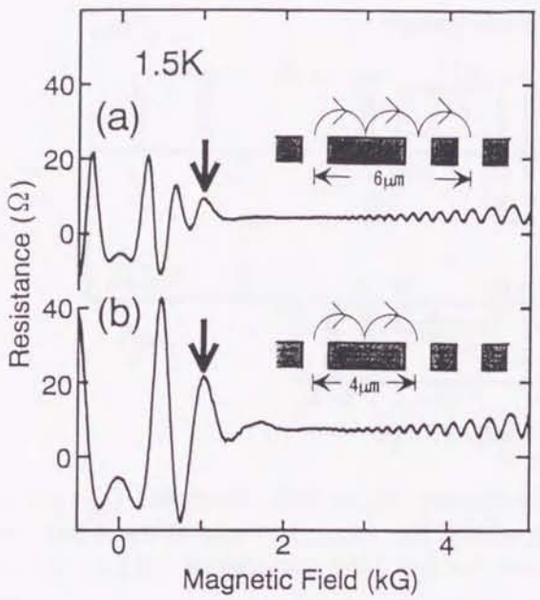

Figure 4.7: (a) Magnetoresistances of ΔL=6 μm with extra probe between E and C separation. Focusing effect via reflection at extra probe is pronounced at the allow. Inset shows schematic trajectory of electrons in the case indicated by the arrow. (b) Conventional electron focusing effect via one-time reflection at the 2DEG boundary (arrow).

enter the extra probe (Fig. 4.7: inset), the focusing peak is also clearly observed (Fig. 4.7(a)). It can be confirmed that the electrons contributing to the focusing peak are coming from the extra probe because its peak magnetic field corresponds to that of $\Delta L = 4\mu$m as shown in Fig.4.7. This extra probe reflection is explained in the following way. The electrons focused on the extra probe pile up there and make the chemical potential of the extra probe higher. This extra probe would emit other electrons, most of which would be emitted near the perpendicular direction to the boundary,[71] then these electrons are focused on the collector by the magnetic field.

4.1.3.4 Electron focusing effect via a byway channel

To confirm the mechanism mentioned above, we made a device with a byway channel as shown in Fig. 4.8.[78] This sample is made from HEMT# 2. The distances of $\Delta L'$ are 3 μm. The length between the emitter (E) and collector (C) is 31 μm, therefore, the electron trajectory (31 μm $\times$ $\pi/2$) is much longer than l_e = 10 μm. At $B_{foc} = 2\hbar k_F/(e \times \Delta L')$, the conventional electron focusing effect occurs between E and byway entrance (W_i) and between byway exit (W_o) and C, simultaneously (Fig. 4.8(b)), because the distances of E-W_i and of W_o-C are the same. When the focusing effect occurs at E-W_i at W_o-C, if the chemical potential of W_i is propagated to W_o through the byway channel, the focusing peak can be observed at E-C. Magnetoresistances due to the focusing effect are shown in Fig. 4.9(a). The peaks are observed as shown in Fig. 4.9(a)(I) in the configuration with a byway. Peak magnetic fields correspond to those of the conventional electron focusing effect with $\Delta L' = 3$ μm (Fig. 4.9(a)(III)). That is, the peak at 0.8 kG stems from the direct focusing effect (B_{foc}) and the one at 1.6 kG one-time reflection at 2DEG boundary (B_{ref}).

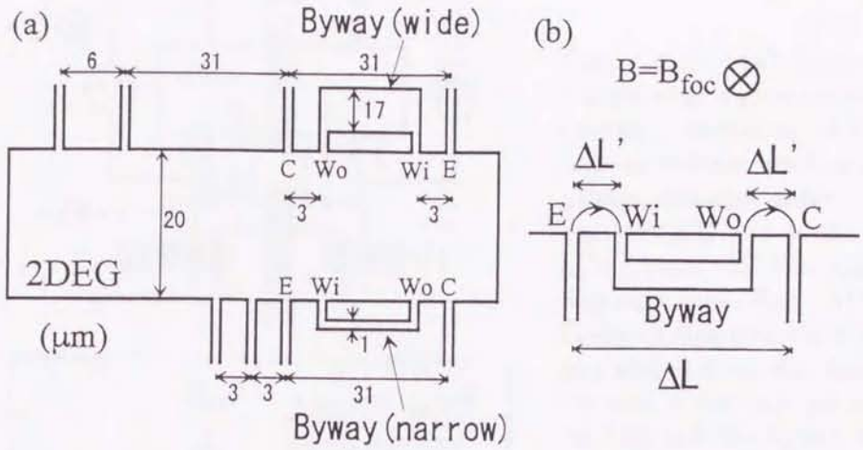

Figure 4.8: (a) Schematic view of the sample with two byway channels. Upper byway is wide (17 μm) and lower is narrow (1 μm). All widths of electrodes is 1 μm. (b) The distances between emitter (E) and byway entrance (W_i) and between byway exit (W_o) and collector (C) are the same at 3 μm.

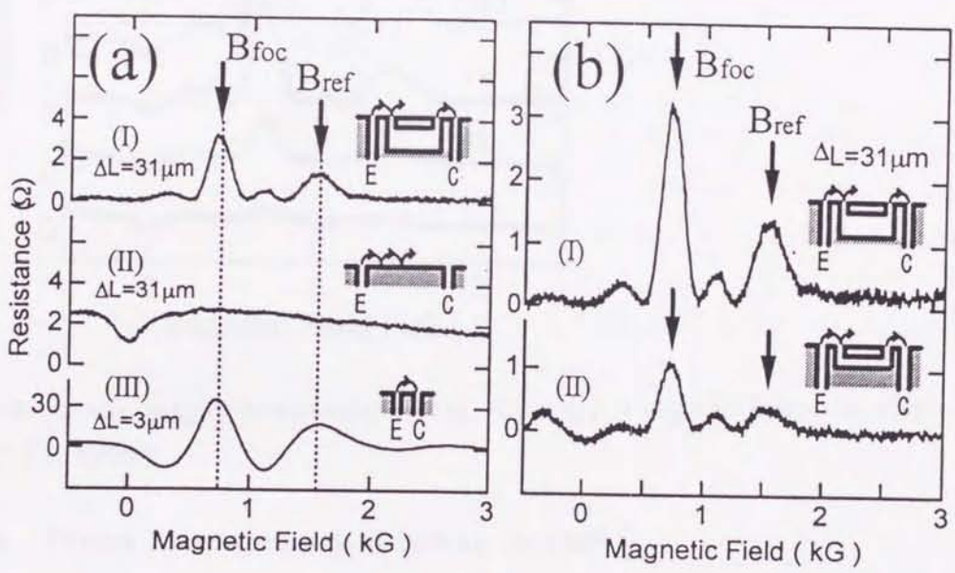

Figure 4.9: (a) Magnetoresistances with wide byway channel (I), without any extra probe (II) and the conventional electron focusing effect (III). (b) Magnetoresistances due to the magnetic electron focusing effect through the wide (I) and narrow byway (II).

The peak magnetic fields agree with the calculated $B_{\rm foc}$ ($= 2\hbar k_{\rm F}/e\Delta L$) and $B_{\rm ref}$ ($= 2 \times B_{\rm foc}$). Obviously, any peaks do not appear without the byway (Fig. 4.9(a)(II)).

We also investigate the dependence of the peak heights on the byway width (Fig. 4.9(b)). The width of wide byway is 17 μm and that of narrow one is 1 μm. The peak through the wide byway is higher than that through the narrow one. This difference is attributed to the resistance of byway. Thus, the focusing peak height may depend on the transmission probability of electrons from W_i to W_o through the byway. Consequently, it is obvious that

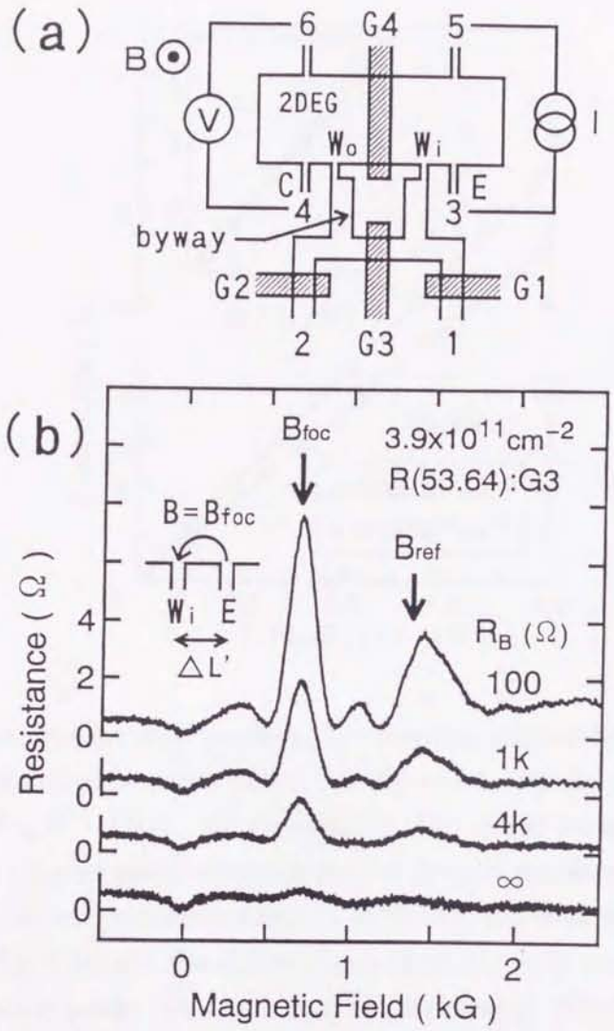

Figure 4.10: (a) Schematic view of sample with a gate-controllable byway channel. Notations "1-6" denote current or voltage probes and "$G1$-$G4$" denote Schottky gates. Probe 3 is an emitter (E), and probe 4 a collector (C). Gate $G3$ can control the byway resistance (R_B). (b) Magnetoresistances of magnetic electron focusing effect with various R_B. Inset: Schematic electron trajectory between the emitter (E) and the byway entrance (W_i) at $B = B_{foc}$.

the peaks in the magnetoresistance of Fig. 4.9(b)(I) is derived from the electrons passing through the byway.

4.1.3.5 Direct measurement of byway current

In order to measure a current through the byway, we made a sample with a gate-controllable byway (Fig. 4.10(a)) from a GaAs/AlGaAs heterostructure (HEMT# 1).[79] Sample was fabricated by the Type B process (p.11). In Fig. 4.10(a), the notations "1-6" denote current or voltage probes and "$G1$-$G4$" denote Schottky gates. In the measurement, we use probe 3 as an emitter (E) and probe 4 as a collector (C). Both distances $\Delta L'$ of E-W_i and of W_o-C are 3 μm. The E-C separation length is 31 μm. The electron path from E to C (=31 μm $\times\pi/2$) is also much longer than the mean free path (18 μm). The geometrical width of the narrow part of the channel is about 1 μm, and that of the wide region is 4 μm. The width of Schottky gates is 8 μm. Applying negative voltage to $G3$, we can control the byway channel resistance. The notation "$R(ij.kl) : Gm$" shows the following

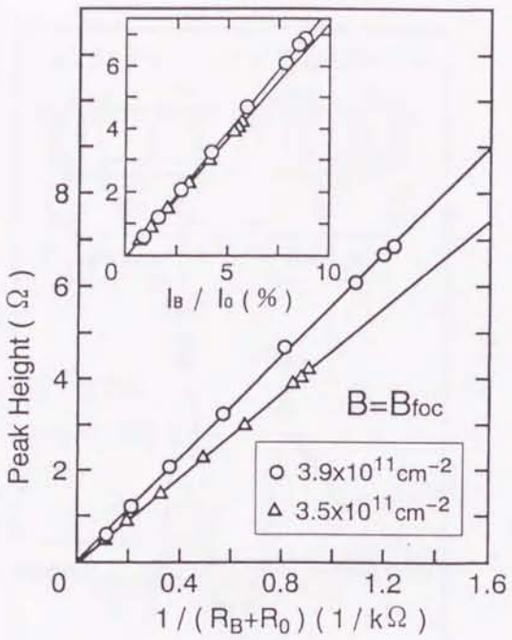

Figure 4.11: Relationship between the peak height at $B = B_{foc}$ and $1/(R_B + R_0)$, where R_0 is the residual resistance of the byway. Inset shows the relationship between the peak height and I_B/I_0, where I_0 is total current from emitter.

measurement configuration; the nominal current flows from probe i to probe j, the voltage is measured between probe k and probe l, and the gate voltage (V_G) is applied to gate Gm. At $V_G = -1.0$ V, the resistance of the byway exceeds 2 MΩ and the byway is pinched off. The unused gates are connected to ground potential.

The magnetoresistances in $R(53.64) : G3$ with various byway resistances (R_B) are shown in Fig. 4.10(b). We define R_B as $R(43.21) : G3$ with pinched-off $G4$ ($V_{G4} = -1.0$ V). Two focusing peaks (B_{foc} and B_{ref}) appear clearly. When the cyclotron diameter of the electrons coincides with $\Delta L'$, the electrons from E are directly focused into W_i (inset of Fig. 4.10(b)).

The peak at $B = 0.7$ kG (B_{foc}) comes from the electrons which are directly focused between E and W_i and between W_o and C. The peak at $B = 1.4$ kG also appears via the one-time reflection at the sample boundary at $B_{ref} = 2 \times B_{foc}$. With increasing R_B, two peaks decrease, and almost vanish when the byway channel is pinched off ($R_B = \infty$).

Now we consider the relationship between the peak height at $B = B_{foc}$ and the byway resistance (R_B). As shown in Fig. 4.11, the peak height is inversely proportional to the total resistance of the byway ($R_B + R_0$), where R_0 is the residual resistance of the byway. The relationship can be explained as follows. At first, we estimate the current in the byway (I_B). By measuring $R(43.21) : G3$ with the pinched off gate $G4$ ($= R_B$) and $R(53.21) : G3$, we obtain I_B/I_0 from the ratio of $R(53.21)/R_B$, where I_0 is the total current from the emitter (inset of Fig. 4.11). Since the resistance of the wide 2DEG region is much lower than that of the byway channel, the potential difference between W_i and W_o is almost constant. The current I_B is inversely proportional to the total resistance of the byway ($R_B + R_0$). The peak height is proportional to $1/(R_B + R_0)$, as shown in Fig. 4.11. The fitting parameter R_0 is 0.7 kΩ at $n_s = 3.9 \times 10^{11}$ cm^{-2} and 1 kΩ at $n_s = 3.5 \times 10^{11}$ cm^{-2}. Resistance R_0 is

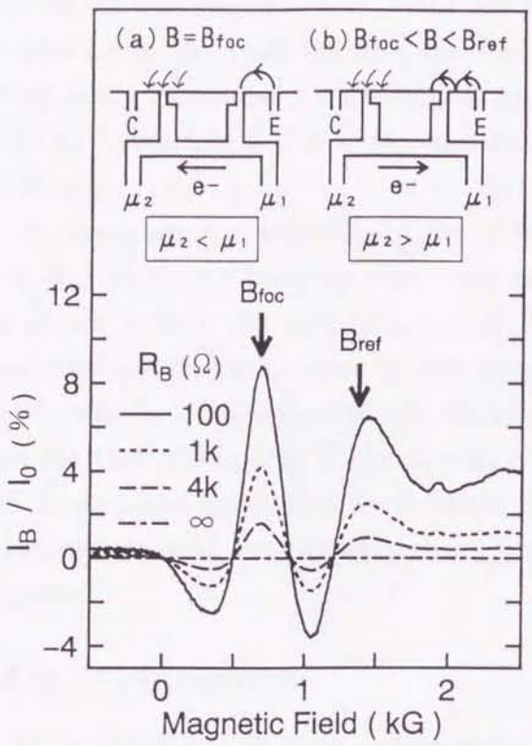

Figure 4.12: Magnetic field dependence of the ratio of I_B to I_0 with various R_B, where I_B is the byway channel current and I_0 is the total current. Inset: Schematic electron trajectory at $B = B_{foc}$ (a) and $B_{foc} < B < B_{ref}$ (b).

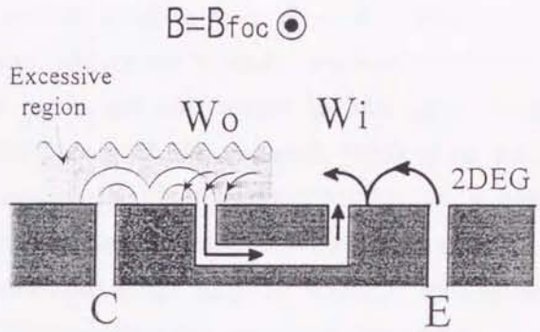

Figure 4.13: Schematic view for understanding an origin of the subpeak. The chemical potential of "electron excessive region" is slightly higher than the Fermi energy.

a reasonable value in comparison to a half of two-terminal resistance between probe 6 and probe 4 (about 1.5/2 kΩ). With larger n_s, the slope increases and R_0 decreases, because the mean free path increases. We conclude that these focusing peaks come from the current through the byway.

Moreover, we investigate the behavior of I_B/I_0 in the magnetic field. Figure 4.12 shows that I_B/I_0 with various R_B oscillates in the magnetic field. The two peaks at $B = B_{foc}$ and B_{ref} decrease with increasing R_B. This trend coincides with the result already shown in Fig. 4.11. Here, we consider the electron flow direction in the byway. At $B = B_{foc}$, the electrons from E are directly focused into W_i and the chemical potential of probe 1 (μ_1) becomes higher than that of probe 2 (μ_2), as shown in inset(a). The electrons (e^-) flow in the byway in the direction of the arrow (inset(a)). At most, about 9 % of the total current I_0 flows in the byway. Because of the angular distribution of emerging electrons from E,[80-86] the scattering on the focusing trajectories,[66,69,70,74] and the reflection at the W_o,[74,78] a small part of the electrons from the emitter contribute to the byway current. In the regions of $0 < B < B_{foc}$ and $B_{foc} < B < B_{ref}$, the electrons from the emitter do not enter W_i, as shown in inset(b). On the other hand, the amount of electrons which enter W_o negligibly

depends on the magnetic field, since the E-W_o distance (28 μm) is much longer than the electron mean free path (18 μm) and the most electrons are scattered before reaching the byway exit. The chemical potential of probe 2 (μ_2) becomes higher than that of probe 1 (μ_1). As a result, in $0 < B < B_{foc}$ and $B_{foc} < B < B_{ref}$, the electrons (e^-) flow inversely in the byway.

Furthermore, the subpeaks in Fig. 4.10(b) are observed in $0 < B < B_{foc}$ and $B_{foc} < B < B_{ref}$ where the focusing effect does not occur. Since such peaks are also observed in the device without the gate (Fig. 4.9(b)),[78] the peaks are not caused by the gate. As we mentioned above, the counter current flows in the byway at the subpeak fields (Fig. 4.12). At W_o, the electrons are pulled into the byway because the chemical potential of W_i is lower than the that of W_o (Fig. 4.13). A part of these electrons emitted from W_i is scattered in 2DEG again and enters into the collector. The electrons enter into the collector excessively in comparison with the case of without byway. These excess electrons are the origin of the subpeaks.

4.1.4 Conclusion

In conclusion, we have investigated the magnetic electron focusing effect in a GaAs/AlGaAs 2DEG with multiprobe. With increasing electron density, the ballistic elastic scattering length increases and the specularity at the sample boundary decreases. Furthermore, even in a configuration where the focused electrons can enter an extra probe located between the emitter and the collector probes, the focusing effect can be clearly observed. By the experiment of the byway, we conclude that the extra probe reflection originates in the re-emission of electrons from the extra probe where the electrons enter by the electron focusing effect.

4.2 Investigation of electron emission distribution from oblique wire

4.2.1 Introduction

When the electron travels adiabatically from the narrow to the wide region in the gradually widening channel (Fig.4.14), the transverse quantum state is conserved. In this situation, its transverse momentum $k_\perp$ is gradually transferred into the longitudinal momentum $k_{||}$, and $k_{||}$ increases. Thus, the electron stream through a narrow channel is collimated in the forward direction of channel, and this effect is called "electron collimation effect". In accordance with the collimation effect, the angular distribution is expected to be narrower as the channel width becomes narrower. In the early stage of this investigation, the various crossed junctions have been studied.[29,30,87-94] The collimation effect is observed as follows: The Hall resistance is suppressed around zero field (quenting of Hall effect),[29,87,88] and "bend resistance" in which the electron stream passed around the corner at a junction is observed.[30] In the calculation by the recursive Green's-function method, Baranger and Stone have showed that generic quenching is found when the width of the wire is gradually increased near the junction to the Hall probes.[91] Beenakker and van Houten have calculated the electron distribution near the orifice of the narrow channel in the classical billiard ball view and also have showed that the rounded corner collimates the electron stream more than the abrupt corner.[93] These effects are interpreted as that at the rounded corner the spreading electrons are bounced back to the forward direction by the rounded wall. Usuki *et al.* have showed, in the calculation, that the existence of the collector also influences the

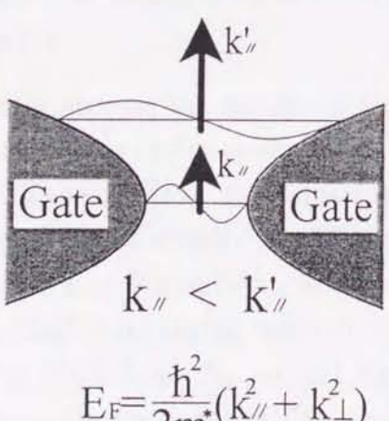

Figure 4.14: Adiabatic propagation of electron wave function through a gradually widening wire. The wavelength along the transverse direction parallel to $k_\perp$ becomes broader as it propagates to wide region.

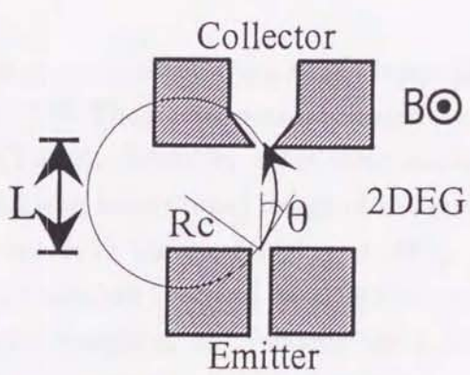

Figure 4.15: Schematic view for an investigation of angular distribution of electron from wire. The relation between the angle (θ) of emitted direction and B is $\theta = \arcsin(eBL/2\hbar k_F)$.

angular distribution of electron stream by the reflections, whereas the fundamental symmetry is conserved.[95] In the recent experiments, the angular distribution is measured in the transfer resistance configuration with a series of emitter (E) and collector (C) point contacts facing each other across 2DEG[80-86,96] (Fig. 4.15). The electron stream from E can enter C because of the overshooting effect of electrons in the high quality 2DEG. By wheeling the electron stream from E in magnetic field (B), the angular distribution of electron stream can be deduced. The relation between the angle (θ) of emitted direction of electron and B is given as $\theta = \arcsin(eBL/2\hbar k_{\mathrm{F}})$, where L is separation length between E and C. Following Cumming *et al.*, however, the angular distribution is destroyed occasionally by the single impurity in front of E or C.[84]

The magnetic electron focusing effect[20,22,61-75] is also useful method to see the electron distribution from a wire. The peak magnetic field is apparently determined by electrons emitted at $\theta = 0°$, where θ is a tilted angle of the emission direction from the channel direction.[71,86]

In this section, we investigate the angular distribution from the narrow oblique wire which is tilted to the 2DEG boundary. In this experiment, it is expected that the peak of magnetoresistance of the transfer resistance would shift from the case of vertical wire if the electron collimation along the wire direction occurs. Moreover, we investigate the electron distribution in magnetic electron focusing effect. The experimental data are also compared with the calculated ones by a classical billiard model.

4.2.2 Results and discussion

4.2.2.1 Direct measurement of angular distribution of electrons from narrow wire

To directly observe the angular distribution of electrons emitted from wires, magnetoresistance is measured in the configuration of Fig. 4.15.[80-85] The device was fabricated by the process of "Type E" from a heterostructure (HEMT# 2). Schottky gates were made by evaporation of Ti/Au metals. The SEM (scanning electron microscope) image of the sample surface is shown in Fig. 4.16(a), and a schematic view is in the inset of Fig. 4.16(b). An upper wire "$E1$" is connected vertically to the 2DEG boundary (*vertical wire*), while a lower wire "$E2$" is tilted from the vertical direction under an angle of 45° (*oblique wire*). Each emitter has a collector across 2DEG away from 4 μm, whose distance is shorter than a mean free path ($\sim$ 6 μm). Resistance was measured at 0.4 K by operating an excitation current 30 nA.

Figure 4.16(b) shows gate-voltage dependence of resistances at zero-magnetic field. The emitter and the collector channels are formed at $V_g \sim -0.6$ V. Since the resistance of wire is much lower than the quantized value $h/2e^2 \sim 12.9$ kΩ, the wire width is much wider than

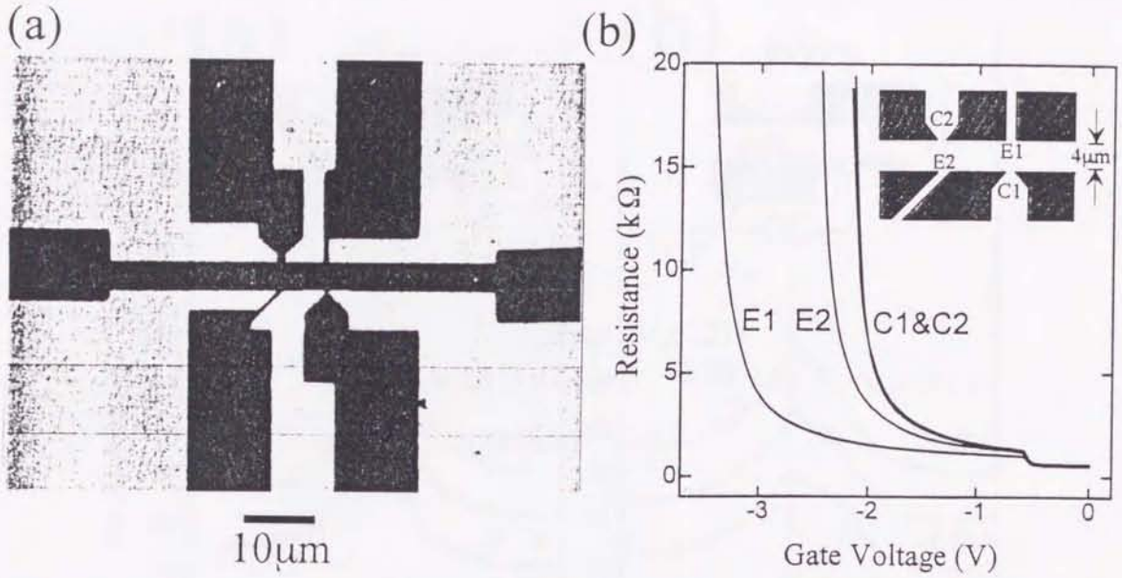

Figure 4.16: (a)SEM image of the surface of device. Gray regions are Schottky gates, and darken regions are connected to ohmic contacts. (b)Two-terminal resistances of each gate. "$E1$" is a vertical and "$E2$" is an oblique emitter wire. "$C1$" and "$C2$" are collector point contacts. Inset: A schematic view of sample.

the Fermi wavelength. So, the electrons will behave like a pinned ball. From the assumption that the resistance is proportional to the ratio of wire width to the length from the resistance at $V_g \sim -0.6$ V, the $E1$ width is estimated as 0.7, 0.6, 0.2 μm at $V_g = -1.0, -2.0, -3.0$ V, and the $E2$ width as 0.4, 0.3, 0.2 μm at $V_g = -1.0, -1.5, -2.0$ V, respectively. The $C1$ width and the $C2$ width are 0.05 μm at the gate voltage $V_g = -2.0$ V.

An angular distribution of emitted electrons from the vertical wire ($E1$) or oblique wire ($E2$) are investigated as shown in Fig. 4.17. The configurations of electrodes are shown in each inset. The magnetoresistances are plotted as a function of θ. In the case of vertical wire (Fig. 4.17(a)), the peaks are almost symmetric in θ. With decreasing gate voltage for $E1$, the angular distribution becomes slightly sharper. This is because the electron angular distribution is slightly collimated along the wire direction. Moreover, the fine structures grow around $\theta = 0°$. The angles of the fine structures does not shift in the different $C1$ width. These may be caused by the electron reflection at the emitter orifice or by the influence of impurities.[80,97] Ando points out that the reflection wave between E and C plays an important role in the electron transport, and it makes a complex shape on the magnetoresistance.[98]

Similarly, the angular distribution from the oblique wire ($E2$) is investigated (Fig. 4.17(b)). If the electrons from $E2$ go straight along the wire direction, the angular distribution would shift by 45° from the vertical direction. In Fig. 4.17(b), however, the measured shift is about 10° from the vertical direction. The result shows that the angular

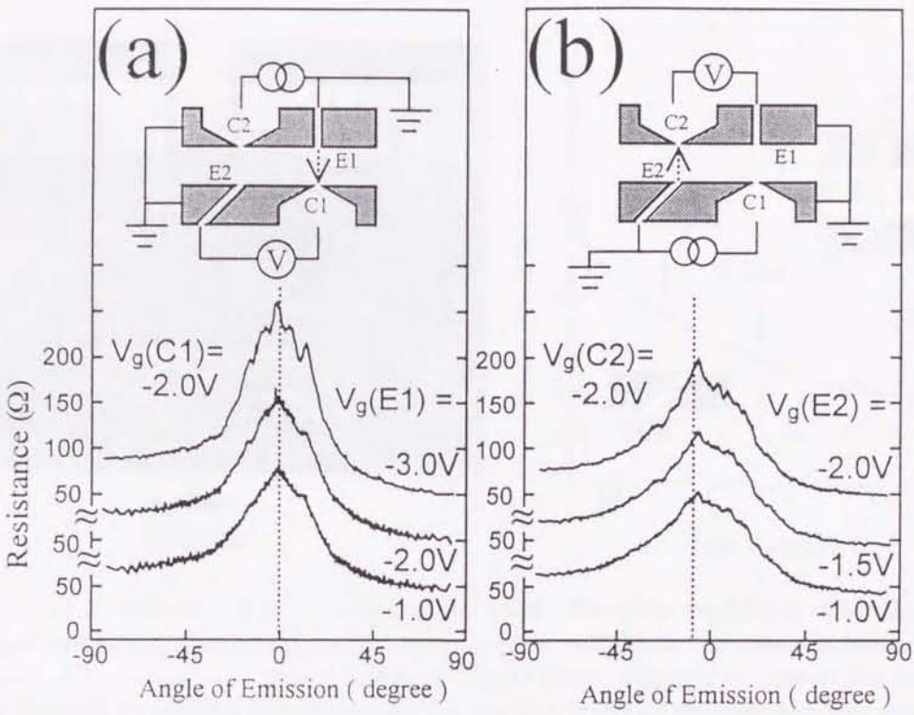

Figure 4.17: The angular distribution of electrons emitted from the vertical probe (a), and from the oblique probe (b). Insets show the configuration of electrodes. Unused two gates were connected to the ground potential.

distribution depends on the wire direction but the value of peak shift is not determined only by the wire direction. Following the consideration by Nixon *et al.*, the random potential causes the wire to break up before it can be made narrow enough to remain lowest subband state.[99,100] In our experiment, some parts of wire may be squeezed by the random potential before wire width reaches narrow enough to collimate the electron stream. Consequently, the angular distribution may depend on the structure just at the orifice of the wire. It should be noted that at the orifice of the oblique probes the escaping electron waves feels asymmetric termination of the wire.

4.2.2.2 Investigation by magnetic electron focusing effect

We also investigate the influence of the peak shift of about 10° in the angular distribution from the oblique wire on the electron focusing effect. A SEM image of a sample is shown in Fig. 4.18(a), and a schematic view in the inset of Fig 4.18(b). The separation ΔL between the emitter and the collector is 6.5 μm. The lower wires are tilted under an angle of $\pm 45°$ from the vertical direction. In the electron focusing effect, the peak shift from oblique wire would be also expected.

Figure 4.18(b) shows the two-terminal resistance of an oblique wire as a function of the gate voltage. Since the 2DEG under the gates is depleted and the wire channel is constructed

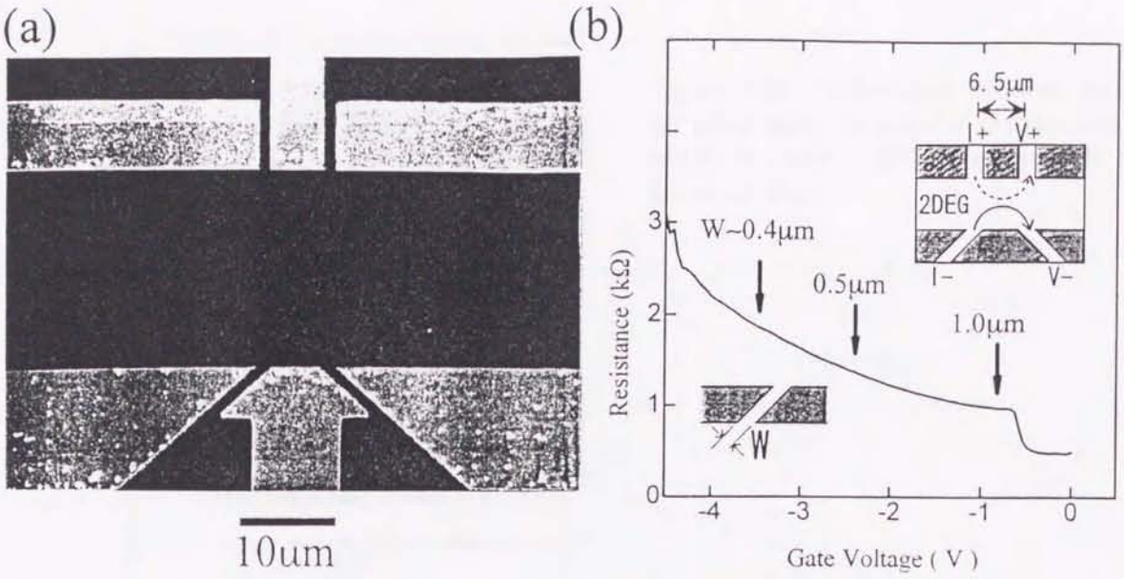

Figure 4.18: (a) A surface image of a sample by SEM. The gray regions is Schottky gates. (b) Two-terminal resistance of an oblique wire versus applied voltage to the gate-electrodes. Estimated widths at each gate voltage are shown in figure. Upper inset: Schematic view of the sample. Solid and broken lines show the electron trajectory for the first peak of the electron focusing effect.

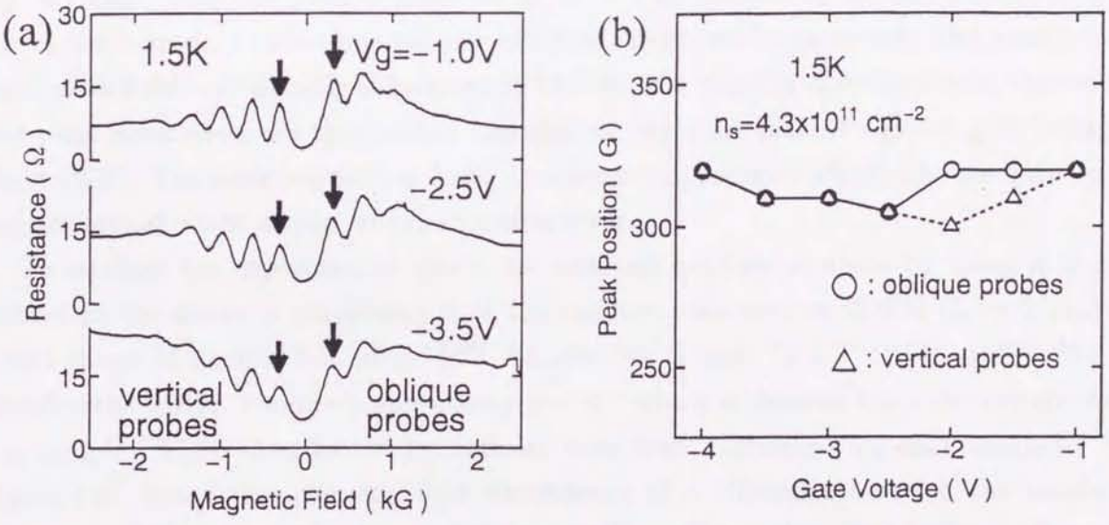

Figure 4.19: (a) Magnetic electron focusing effect at three gate voltages. The electron focusing effect with vertical probes appears in the region of negative magnetic fields, while that effect with oblique probes in positive magnetic fields. The arrows indicate the positions of first peak. (b) First peak positions at various gate voltages.

at gate voltage $V_g = -0.6$ V, the channel width could be estimated at 1.0 μm which is the gap width in the SEM image. Since the wires are much wider than the Fermi wavelength and have dozens of subbands in each wire, the electrons behaves like a pinned ball. From an assumption of the proportional relation between the conductance and the wire width, the wire widths are 1.0, 0.5 and 0.4 μm at $V_g = -1.0$, -2.5 and -3.5 V, respectively.

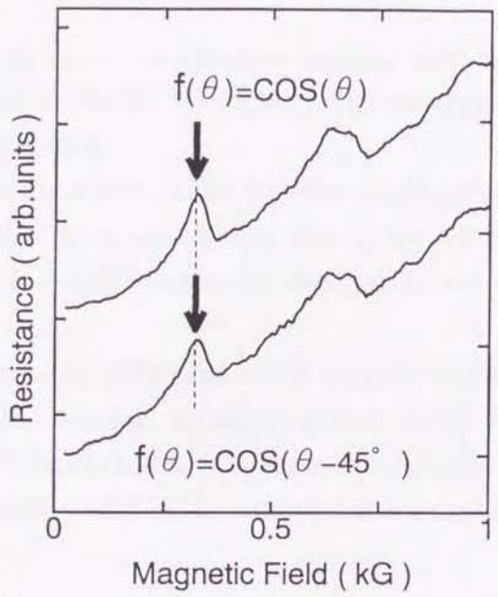

Figure 4.20: Calculated electron focusing effect with the angular distribution of $cos(\theta)$ or $cos(\theta - 45°)$. Broken lines are drawn at $B_{\rm foc}$.

The magnetoresistances due to the magnetic electron focusing effect are shown in Fig. 4.19(a). The *first peak* is observed at $B \sim B_{\rm foc}$ (shown by allows) and some peaks due to the boundary reflections are also observed. Here, we focus on only first peak because these peak fields are directly influenced by the electron angular distribution at the emitter. The peak positions from the vertical and oblique wires are plotted against gate voltage in Fig. 4.19(b). The peak positions in both sides are not apparently affected by the gate voltage and are almost same within an experimental error.

To confirm the experimental result, we simulate electron motions by using a classical billiard model under a consideration of the random scatterers in 2DEG ($l_{\rm e} \sim 7$ μm) and a real shape of sample boundary.[93,94] An electron density is 4.3×10^{11} cm^{-2}. We also consider the 2DEG boundary specularity $p \sim 0.7$ which is derived from the experiment of this sample. More than $5{\times}10^3$ trajectories have been calculated for each magnetic field. Figure 4.20 shows the magnetic field dependence of a difference between the number of electrons entering the probe $V+$ and the probe $V-$. The broken lines indicate $B_{\rm foc}$ where the electrons emitted to the vertical direction are focused. The position and shape of the first peak in $f(\theta) = cos(\theta)$, are almost the same as those in $f(\theta) = cos(\theta - 45°)$. If a collimation occurred, the peak from oblique wire would shift significantly. Because the peak shift from the oblique wire tilted under 45° is not clear in the focusing calculation, the influence by the emission shift under 10° cannot be observed in the focusing experiment (Fig. 4.19). Consequently, no experimental peak shift in the magnetic electron focusing effect can be observed if the remarkable collimation does not occur.

4.2.3 Conclusion

In conclusion, the electron angular distributions from narrow oblique wires, which are connected to the 2DEG region under an angle of 0° (vertical wire) and 45° (oblique wire), are investigated.

In the measurement by transfer resistance configuration, we find that the shift of electron distribution from the oblique wire is not 45° but about 10°. The reason may be that the angular distribution strongly depends on the orifice structure of the wire rather than the wire direction.

From the investigation of the magnetic electron focusing effect, both peak positions from oblique and vertical wires are almost same. We also calculate the focusing effect with a classical billiard model. The experimental peak shift can be observed in the magnetic electron focusing effect only if the remarkable collimation occurs.

4.3 Transport property in antidot lattice

4.3.1 Introduction

Electron transport in lateral antidot superlattices, in which the potential modulated pillars (antidots) are regularly superimposed on the two-dimensional electron gas (2DEG), has been attracting much attention in recent years.[35,101-129] In the antidot lattice, various phenomena, e.g., the Aharonov–Bohm (AB) effect,[101-103] the Al'tshuler–Aronov–Spivak (AAS) effect,[104] and the negative magnetoresistance due to the weak localization by the specular scattering at antidot walls,[127-129] have been observed. In low magnetic fields, some maxima in the magnetoresistance appear.[35,105-118] The magnetic fields of the peaks almost correspond to the cyclotron motion (cyclotron diameter=$2R_c$) with the encircling orbit around some antidots. The oscillations are called "commensurability oscillations", which have been intuitively interpreted by the trapped electrons on pinned electron orbits around some antidots (Appendix A).[105,106] However, in an antidot lattice composed of anisotropic unit cell; e.g., a rectangular cell, the peak magnetic fields depend on the current flow direction.[107-110] This anisotropy dependence can not be explained by the pinned electron orbit model because in the pinned electron model the electrons should be trapped around the antidots irrespective of the current flow direction. Theoretically, Fleischmann *et al.*[119] have solved the classical equations of electron motion and have applied the linear response relation[18] to the square antidot lattice (Appendix A). The result of the calculation suggests that the commensurability oscillations are not caused by the varying of pinned orbits, but by correlations within the chaotic trajectories.

In this section, we consider in more detail the relation between the commensurability oscillations and the current flow direction in anisotropic antidot lattices where the fluctuations either parallel or perpendicular to the current flow direction is introduced into antidot locations. We also investigate various rectangular or isosceles triangular lattices.

4.3.2 Potential modulation on 2DEG (sample preparation)

Our devices are fabricated from a wafer of GaAs/AlGaAs heterostructure (HEMT# 2). The electrons are confined to a 2DEG about 60 nm beneath the surface. Antidot structures are made by the technique of "trench etching"(Type D). After the writing of the dots by EB-lithography on the PMMA resist which was coated on the mesa-etched Hall bar, the patterns were transferred to the heterostructure by the bombardment using 1 kV Ar ions. The etched hole depth was about 15 nm. Since the accelerated Ar ions penetrated well beyond 100 nm from the sample surface, many defects were introduced, and electrons were trapped there.[50,51,57] The carrier density was also changed by the modified potential profile when the cap layer was removed. Thus, the areas of 2DEG under the etched holes were

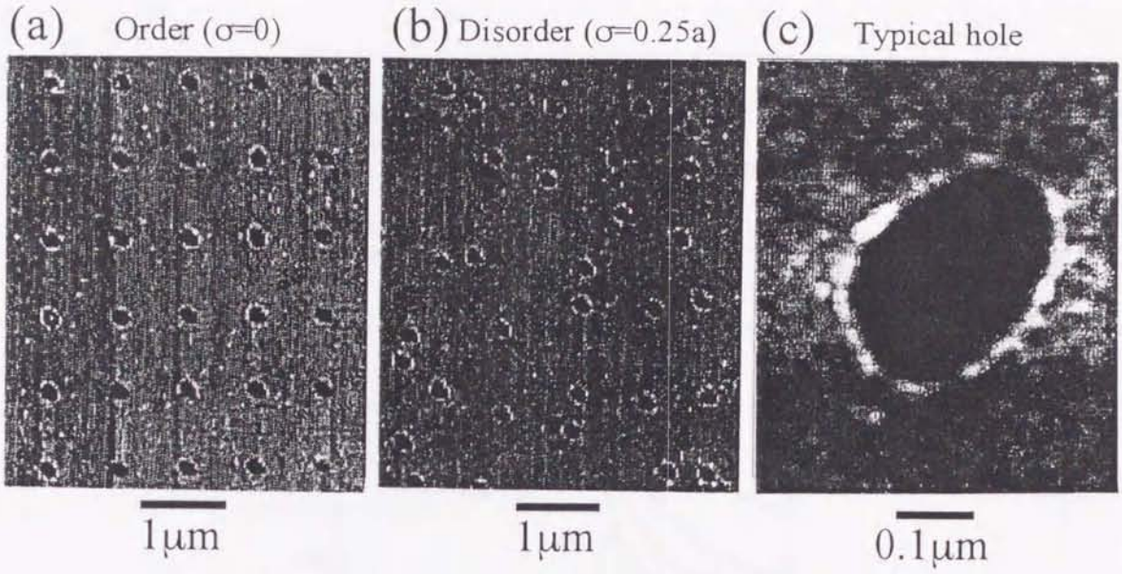

Figure 4.21: Images of sample surface of Fig.4.24. These are observed by atomic force microscope (AFM). Ordered square lattice (a) and disordered lattice (b). Fundamental period (a) is 0.8 μm and antidot diameter is about 0.15 μm. The disorder due to Gaussian distribution (standard deviation=σ) is introduced into the antidot location. In this picture, $\sigma = 0.25a$. (c) Enlarged image of typical hole for an antidot.

depleted and "antidots" were constructed. The images of the sample surface by atomic force microscope (AFM) are shown in Fig. 4.21. Although the circumferences of the holes are not perfect circle and the shapes of individual one in the sample surface differ, the boundary of the depleted area in 2DEG may be smoother than the surface holes, because the 2DEG plane is located at several nano-meter beneath the holes and the depletion layer spreads around the antidot. In order to measure the smoothness of 2DEG boundary, we appraise the specularity by the magnetic electron focusing effect.[69,70,73,74] In one sample, the device for the magnetic electron focusing effect and that for the commensurability oscillations are contained: The device for the focusing effect is about 20 μm away from the antidot lattice whose commensurability oscillations are shown in Fig 4.22. From the dumping ratio of the focusing peaks through the boundary reflection, more than 70% of electrons are bounced specularly by the 2DEG boundary. Thus, the specularity of antidot boundary, which are made in same fabrication process, may also exceed 0.7.

There are two or five antidot regions in the same device. It is desirable that the peaks due to the commensurability oscillations are compared in one sample, because the peaks strongly depend on the antidot diameter[105,110] as shown in Fig. 4.23. The antidot period is changed from 1 μm to 4 μm, and the antidot diameter 0.2-1.2 μm in the ordered triangular antidot lattices. The typical antidot arrays are shown in the upper illustration of Fig. 4.23(a) and (b). The peak heights drastically depend on the ratio of antidot diameter to the period. The peak amplitude of the oscillations also depends on the carrier density (Fig. 4.22). Moreover, the

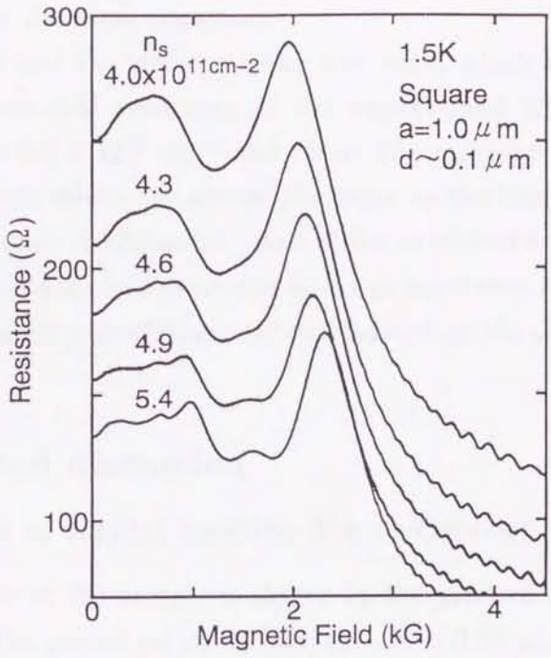

Figure 4.22: Magnetoresistance at various carrier density (n_s). Antidots form square lattice (a = 1 μm, d = 0.1 μm). Carrier density is controlled by the persistent photo conductivity effect under the light from LED (see p.9).

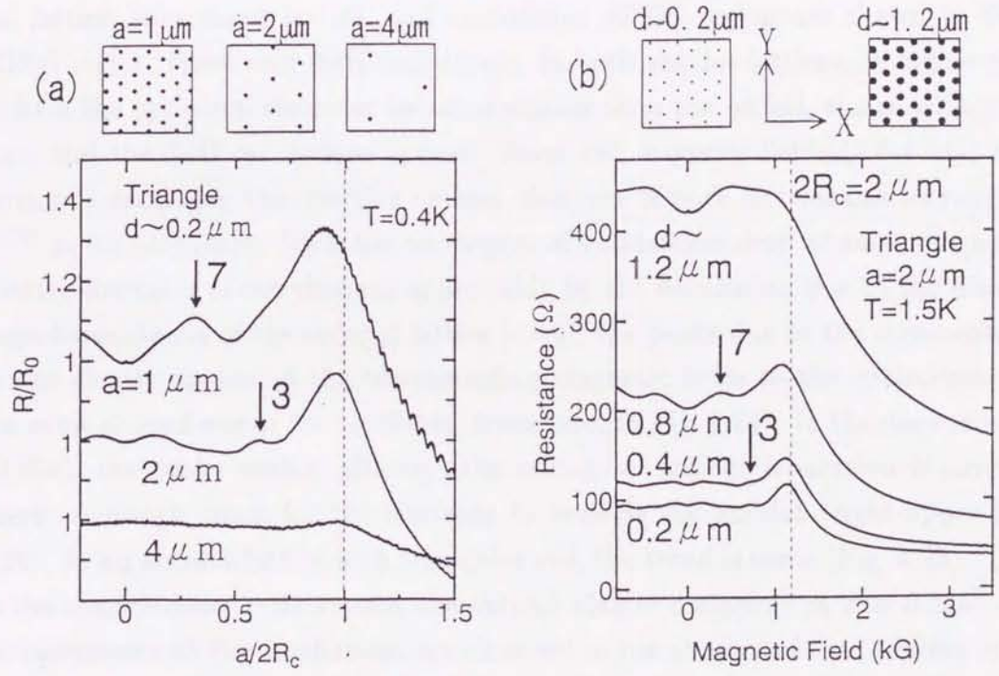

Figure 4.23: Magnetoresistance for various antidot arrays. Period dependence (a), and diameter dependence (b). R_C is cyclotron radius. The dependence on the ratio of the diameter to the period is measured in one sample.

antidot diameter is easily varied by slight change in the fabrication process. It is necessary to measure them under the same condition.

The carrier density and the electron mean free path, which are deduced from the SdH oscillations and the zero-field resistance in the unpatterned 2DEG region in the sample (inset of Fig. 4.24), are 5.2×10^{11} cm^{-2} and about 12 μm, respectively, at 1.5 K and under illumination. Since these values are almost the same as the intrinsic values of the starting heterostructure in the same environment, most of the accelerated Ar ions stop in the PMMA resist. The magnetoresistance was measured by an ac resistance bridge at 15 Hz. The peaks due to the commensurability oscillations did not depend on the current level between 30 nA and 1 μA.

4.3.3 Results and discussion

4.3.3.1 Fluctuation of antidot location due to disorder

The schematic view of the sample is shown in the inset of Fig. 4.24. A fundamental unit cell is a square. The period (a) of the antidot cell is 0.85 μm and the designed antidot diameter (d) is 0.1 μm. We introduce the fluctuations to all directions of antidot location[114] in the Gaussian distribution (standard deviation = σ, a typical antidot group is shown in the right-upper frame of the inset of Fig. 4.24). In the disordered antidot lattice, σ is one-quarter of the lattice period. Antidot areas are 170 μm $\times$ 150 μm. The magnetoresistances of the ordered lattice, disordered lattice, and unmodified 2DEG region are shown in Fig. 4.24. The 2DEG region shows only SdH oscillations. In both antidot lattices, at higher magnetic fields where the cyclotron diameter becomes smaller than the period, the resistance rapidly decreases and the SdH oscillations appear. From the magnetic fields (3.5-4 kG) at which the resistance decreases, the effective antidot diameter of both lattices can be roughly estimated[122] as 0.14-0.17 μm. Since the resistances of two lattices drop at same magnetic field, the effective diameter is not changed appreciably by the fluctuation due to the disorder. In the magnetoresistance of the ordered lattice (σ=0), the peaks due to the commensurability oscillations clearly appear at the corresponding magnetic fields to the encirclement of the electron orbit around one or four antidots (lower inset in Fig. 4.24). In the disordered lattice ($\sigma = 0.25a$), the peaks vanish, although the average of antidot separation is almost same and there is enough space for the electrons to encircle the antidot (right-upper frame of Fig. 4.24). In an antidot lattice with triangular cell, the trend is same (Fig. 4.25). The peak due to the encirclement orbit around one antidot almost disappear at $\sigma = 0.25a$. As a result, no commensurability oscillations are observed in the absence of the ordering of antidot location.

Moreover, we investigate the directional dependence of the fluctuation with respect to the current flow direction. The fluctuation is introduced either in the X-direction (X-disorder)

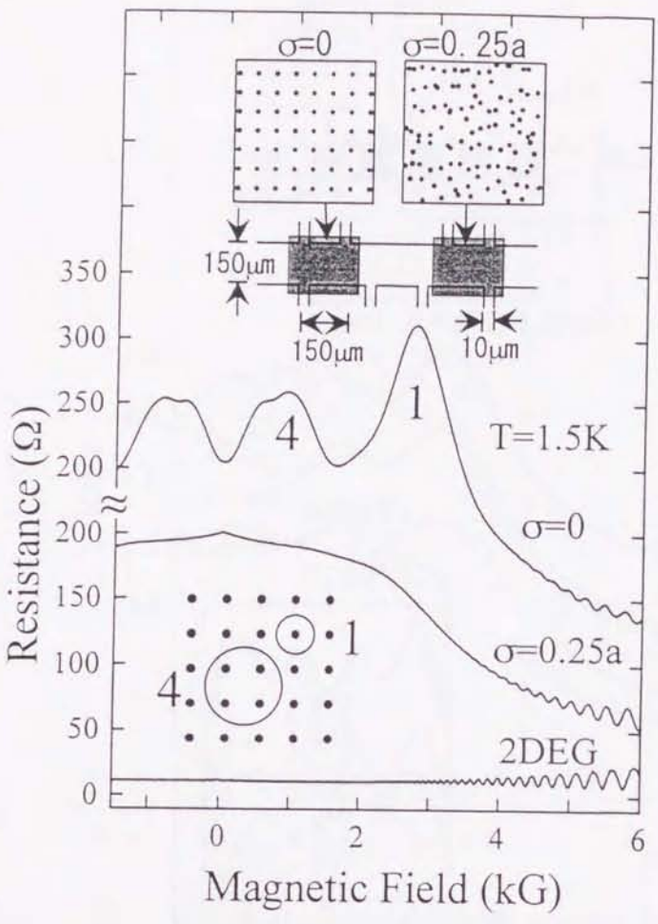

Figure 4.24: Magnetoresistances of the ordered (σ=0) and disordered (σ = 0.25a) antidot lattice, and unpatterned region (2DEG). The fundamental antidot cell is square. The schematic pinned electron orbits (lower inset) correspond to the two maxima (1 and 4) in the magnetoresistance. Upper inset: Sample layout. The two frames of this inset are typical parts of respective antidot lattices.

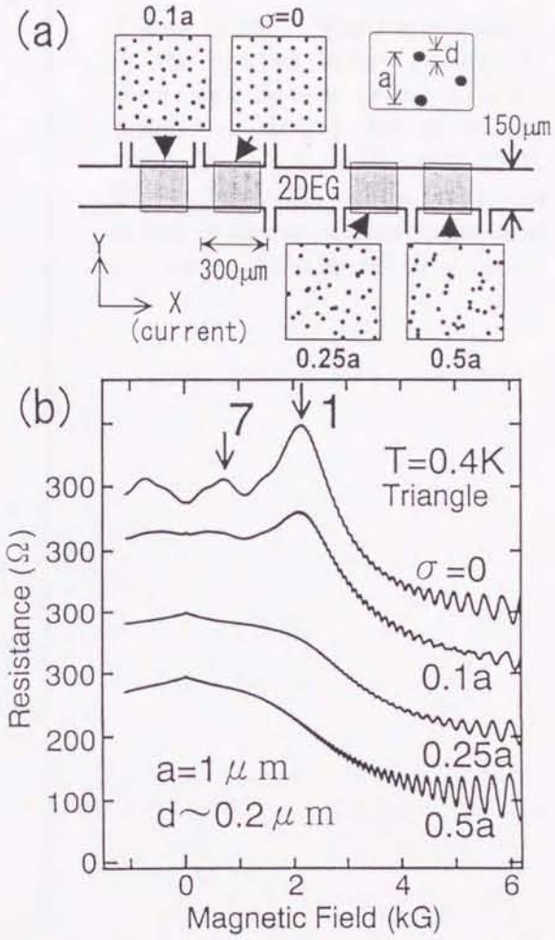

Figure 4.25: (a) Schematic view of sample. There are five antidot lattices in the same sample. (b)Magnetoresistances of triangularly arranged antidot lattices with various standard deviation (σ). With increasing σ, the peak of the commensurate oscillations fades out.

or in the Y-direction (Y-disorder) (upper inset of Fig. 4.26). The X-direction is parallel to the current flow direction. The period is 1 μm and the designed diameter is 0.15 μm. The value of σ is 0, 0.1a, or 0.25a.

The magnetoresistances of these antidot lattices are shown in Fig. 4.26. In the ordered antidot lattice (σ=0), two peaks due to the commensurability oscillations clearly appear. It is surprising that the clear peaks are observed the X-disordered lattices (0.1$a(X)$, 0.25$a(X)$) in spite of the fact that the all-directional fluctuation with σ = 0.25a suppresses the peak as shown in Fig. 4.24. We also find that the amount of decrease depends on the direction

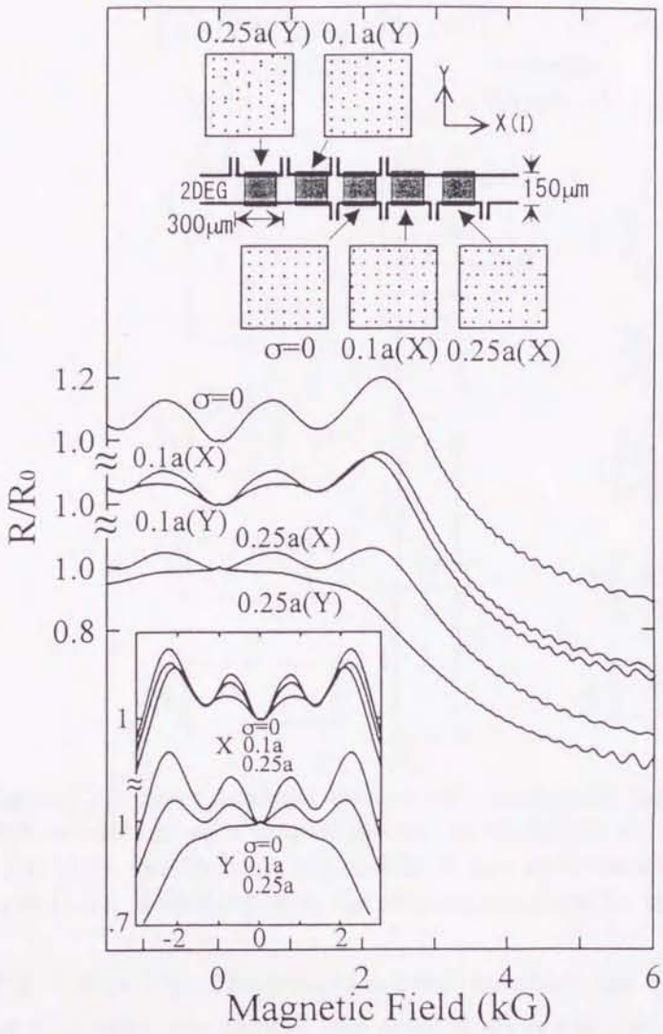

Figure 4.26: Magnetoresistances of the ordered lattice (σ=0), X-disordered lattices (σ = $0.1a(X)$, $0.25a(X)$), and Y-disordered lattices (σ = $0.1a(Y)$, $0.25a(Y)$). Lower inset shows the replotted traces of above magnetoresistances in a series of fluctuated directions.

of the antidot fluctuations. The peaks in the X-disordered lattices ($0.1a(X)$, $0.25a(X)$) are higher than those in the Y-disordered lattices ($0.1a(Y)$, $0.25a(Y)$). The replotted traces in the lower inset of Fig. 4.26 show the situation more clearly. Because the X-direction and the Y-direction are originally equivalent in the square lattice and the X-disordered lattice and Y-disordered lattice are essentially equivalent under 90° rotation, the commensurability oscillations of the two lattices must be the same in the light of the pinned electron model where the current flow direction is not considered.[105]

4.3.3.2 Anisotropic antidot lattice with rectangular or isosceles triangular cell

To confirm the importance of the order along the Y-direction, we investigate the several antidot lattices with rectangular or isosceles triangular cell. Fundamental cell in each lattice is shown in Fig. 4.27. The ordered 9000 antidots are arranged in each lattice.

Figure. 4.28 shows the magnetoresistances in the several rectangular antidot lattices. Figure 4.28(a) presents the magnetoresistances of antidot lattices with several a_x at a_y=1 μm

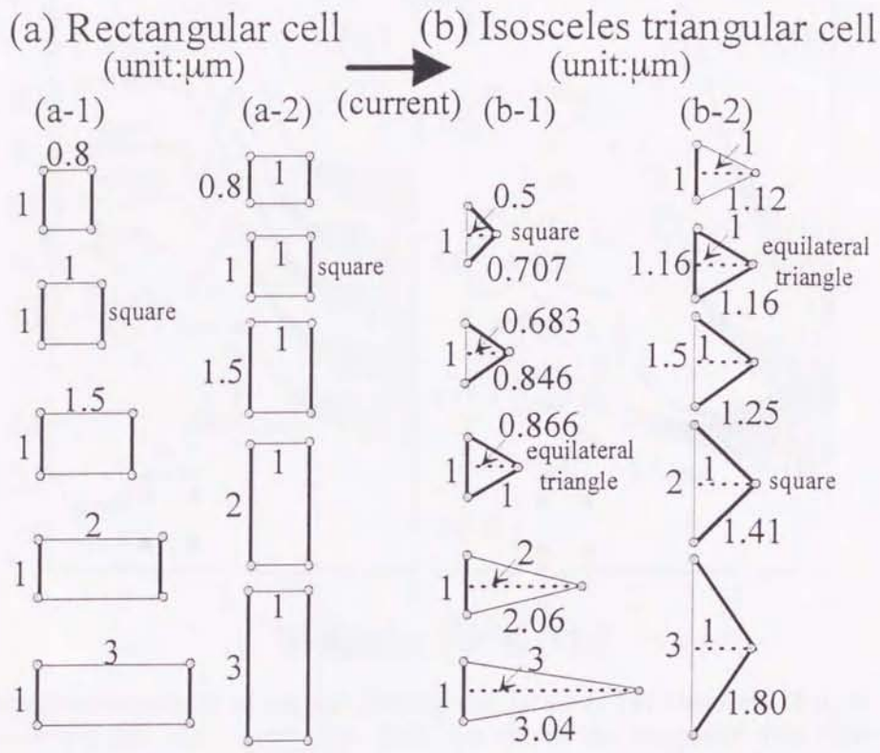

Figure 4.27: Several antidot lattices with rectangular (a) or isosceles triangular cell (b). There are 9000 antidots in each antidot lattice. In the lattice with rectangular cell, a_y is 1 μm (a-1), or a_x 1 μm (a-2). Similarly, in the antidot lattice with isosceles triangular cell, a_y is 1 μm (b-1), or a_x 1 μm (b-2). Bold lines show the effective distances for the main peaks.

(Fig. 4.27(a-1)). The principal peak, at which the cyclotron motion is commensurate with the circumference around one antidot, does not shift in spite of varying a_x from 0.8 μm to 3 μm. A bold line in Fig. 4.28(a) shows a magnetic field predicted from $2R_c$=1 μm($=a_y$), which agrees with the peak position. However, in the 90° rotated antidot lattices, in which a_x is 1 μm and a_y varies between 0.8 μm and 3 μm (Fig. 4.27(a-2)), the commensurate peak shifts drastically to low fields with increasing a_y (Fig. 4.28(b)). The peak magnetic fields are in close agreement with the magnetic fields predicted from each $2R_c = a_y$.

In the triangularly arranged antidot lattices, however, the peak magnetic fields are not determined only by a_y (Fig. 4.29). In Fig. 4.29(a), a_y is 1 μm and a_x varies (Fig. 4.27(b-1)). The main peak does not shift for a_x = 0.866-3 μm. In these three antidot lattices ($a_y \leq \sqrt{{a_x}^2 + (a_y/2)^2}$), the nearest neighbor distance between antidots are the same (a_y = 1 μm). In other antidot lattices of a_x = 0.683 μm and 0.5 μm ($a_y > \sqrt{a_x^2 + (a_y/2)^2}$), the peak shifts to higher magnetic field. In the squarely arranged lattice (a_x = 0.5 μm), the nearest neighbor distance is the side ($1/\sqrt{2}$ μm) of square, not the diagonal (a_y = 1 μm). These effective distances are presented by bold lines in Fig. 4.27(b-1). The results indicate that the nearest neighbor distances determine the commensurate condition. Similarly, in the

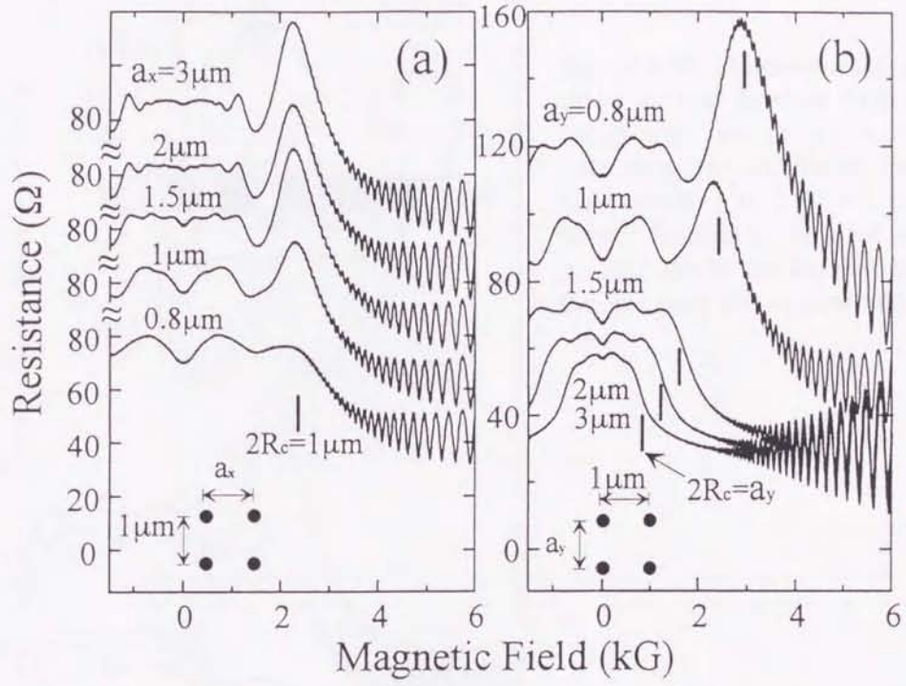

Figure 4.28: Magnetoresistances of various rectangular lattices. (a) Distance of a_y is 1 μm, and a_x varies between 0.8 μm and 3 μm. The bold line shows the magnetic field calculated from $2R_c = 1$ μm. (b) Distance of a_x is 1 μm and a_y varies between 0.8 μm and 3 μm. Each bold line shows $2R_c = a_y$. Insets show a_x or a_y.

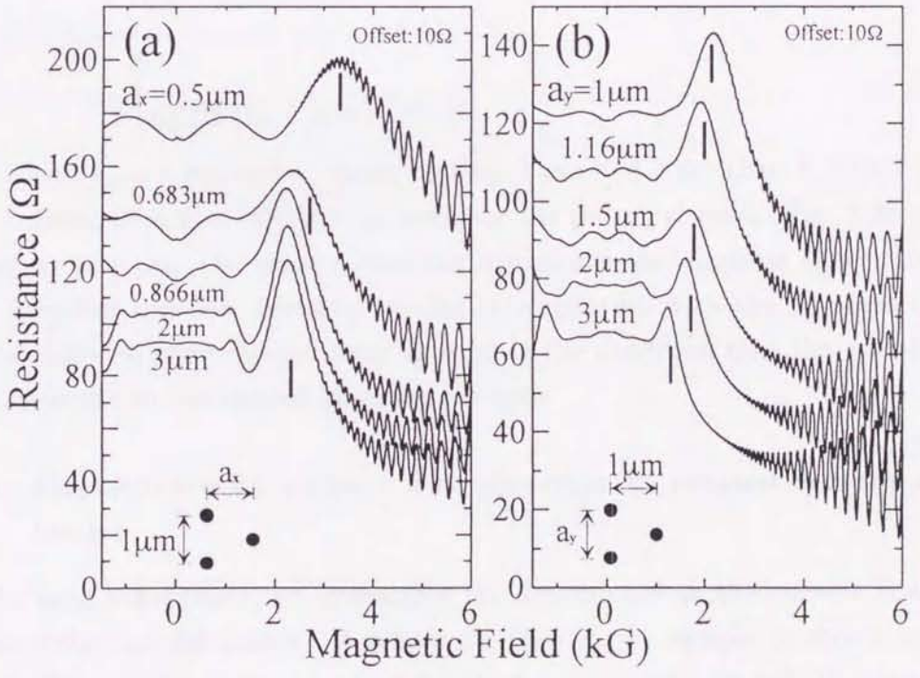

Figure 4.29: Magnetoresistances of several antidot lattices with isosceles triangular cell. The bold lines show the magnetic fields where $2R_c$ is equal to the nearest neighbor distance between the antidots. (a) Distance of a_y is 1 μm, and a_x varies between 0.8 μm and 3 μm. (b) Distance of a_x is 1 μm and a_y varies between 0.8 μm and 3 μm. Insets show a_x or a_y.

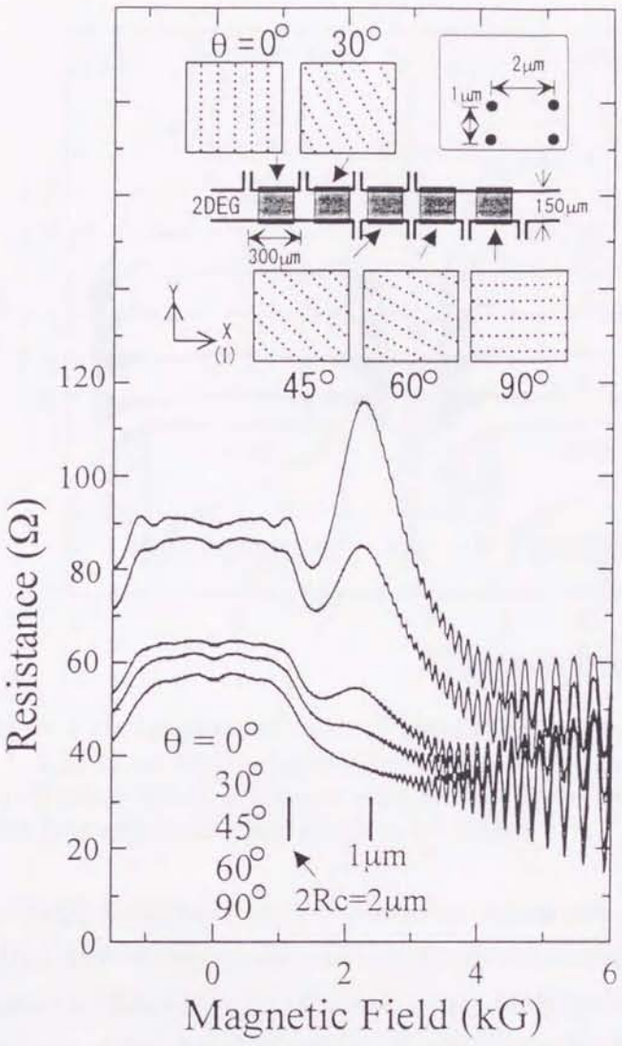

Figure 4.30: Magnetoresistance of various tilted antidot lattices from fundamental rectangular one (2 μm $\times$ 1 μm). Bold lines show the calculated magnetic fields corresponding to $2R_c$ = 1 μm and 2 μm. Inset: Schematic view of sample. The X-direction is the current flow direction. Frames show the typical antidot regions.

lattices where a_x is 1 μm and a_y varies between 1 μm and 3 μm (Fig. 4.27(b-2)), the nearest neighbor distance is also effective in emerging the principal peak (Fig. 4.29(b)). Without lattice of a_y = 1 μm, the nearest neighbor distance is the diagonal ($\sqrt{a_x^2 + (a_y/2)^2}$). The nearest neighbor distance becomes smaller in correlation with the decrease of a_y. In the triangular lattices, the principal peak appears in the condition that the cyclotron diameter is commensurate to the nearest neighbor distance.

4.3.3.3 Dependence on current flow direction in rotated rectangular antidot lattice

In the next experiment, we investigate the dependence on the current flow direction in the rectangular antidot lattice. A schematic view of the sample is shown in the inset of Fig. 4.30. The antidot lattices are composed of rectangular unit cells (2 μm$\times$1 μm) where the longer side of a fundamental cell (θ= 0) is parallel to the current flow direction. The lattices are rotated in five tilted angles (θ=0-90°) as shown in the inset of Fig. 4.30. There

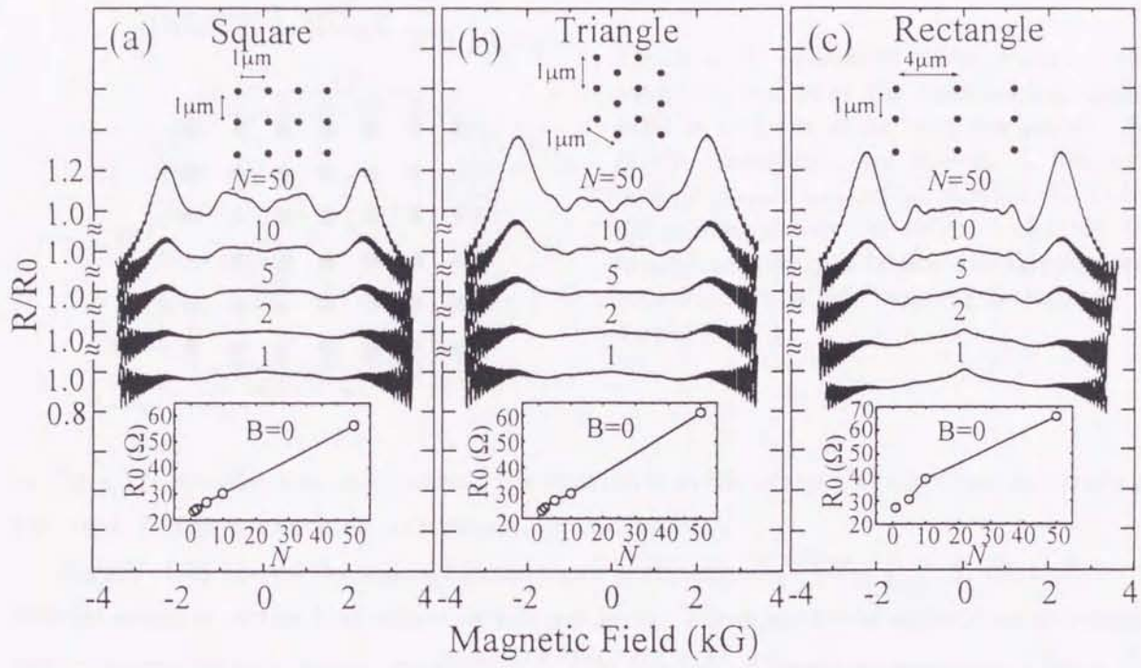

Figure 4.31: Magnetoresistance of various line numbers of antidot arrays (N). The line number N is 1, 2, 5, 10, or 50. Fundamental cell of the antidot lattice is square (a), triangle (b) or rectangular (c). Typical arrays of the lattices and the defined lengths are shown in upper inset. Lower inset: Zero-field resistance (R_0) of each antidot lattice.

are 9000 antidots in each segment of the sample. In the magnetoresistance of the antidot lattice at θ=0, the peaks due to the commensurability oscillations appear when the cyclotron diameter ($2R_c$) is 1 μm, 2 μm or 3 μm. Each cyclotron diameter corresponds to the integral multiple of the lattice period of the shorter side. Bold lines in Fig. 4.30 show the calculated magnetic fields corresponding to $2R_c$=1 μm and 2 μm. Except for the antidot lattice of θ= 90°, the peak of $2R_c$= 1 μm appears at all angles, but decreases with increasing θ.

Moreover, we pay attention to the zero-field resistance. With increasing θ, the zero-field resistance decreases (Fig. 4.30). Few electrons can go through the antidot area without being scattered by the antidots because the length of antidot segment (120 μm) is much longer than the electron mean free path (12 μm). The electrons selectively flow along the wide channel rather than along the narrow channel. The result shows that the resistance of the antidot area is not determined by the density of antidots, but by the channel width along the current flow direction.

4.3.3.4 Antidot array number dependence

In order to examine the dependence of the peak of the commensurability oscillations on the lattice size, we change the antidot array number (N) along the X-direction (=the current flow direction; Fig. 4.31). If the electrons traveling complexly (e.g., the trajectory II

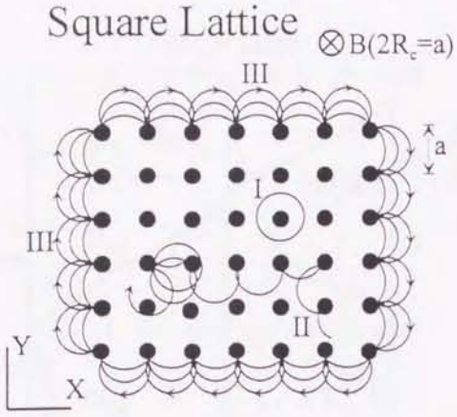

Figure 4.32: Schematic electron trajectories in square lattice when the semiclassical cyclotron orbit is commensurate with the period. Some of the trajectories are shown: I. Steady trajectory pinned around an antidot, II. ordinary diffused trajectory on which a electron travel around complexly in lattice, III. skipping trajectory which is called "runaway trajectory". (See Appendix A.)

in Fig.4.32) are effective and increase the resistance of the system at the commensurate peak, the peak height is expected to strongly depend on N.

Figure 4.31 shows the magnetoresistances with several N (N= 1, 2, 5, 10, and 50). The antidot number in the Y-direction is 150 per array. There are three antidot arrangements of the fundamental cell: square arrangement (Fig. 4.31(a)), triangle arrangement (Fig. 4.31(b)) and rectangular arrangement (Fig. 4.31(c)). At N= 1, three types are coincident. Zero-field resistances (R_0) are shown in the insets. The resistance R_0 is in linear proportion to N. At N= 50 in square lattice (Fig. 4.31(a)), some peaks due to the commensurability oscillations appear, and their heights decrease with decreasing N. However, even at N= 1, the peaks do not vanish. The tendency is similar in other lattices (Fig. 4.31(b) and (c)). In single antidot array, the complex trajectories such as trajectory II is absent. In this single array lattice, following the suggestion by Baskin *et al.*,[120] the "runaway trajectories" (trajectory III) are only considered as the chaotic trajectories. In rectangular lattice with 50 antidot arrays (Fig. 4.31(c)), complex trajectories (trajectory II) are also not so considerable, because the separation between the adjacent antidot arrays are enough large in comparison with the electron cyclotron diameter at the main peak. In the square lattice with N= 50, however, we cannot distinguish the contributions to the commensurability oscillations from the runaway trajectories or the complexly traveling trajectories, and cannot distinguish the two runaway trajectories along X- or Y-direction.

4.3.3.5 Conductivity in antidot lattice

Because the electron stream responds to the externally applied electric field linearly through the conductivity tensor, if we get the conductivity of the system, we can imagine the electron stream. Thus, we convert the experimental resistivity into the conductivity[111] as shown in Fig. 4.33 and Fig. 4.34.

In the square lattice ($a = 1\mu$m, $d \sim 0.1\mu$m; Fig. 4.33), we consider conductivities σ_{xx} and σ_{xy}, which are calculated from the standard formula for the homogeneous two-dimensional

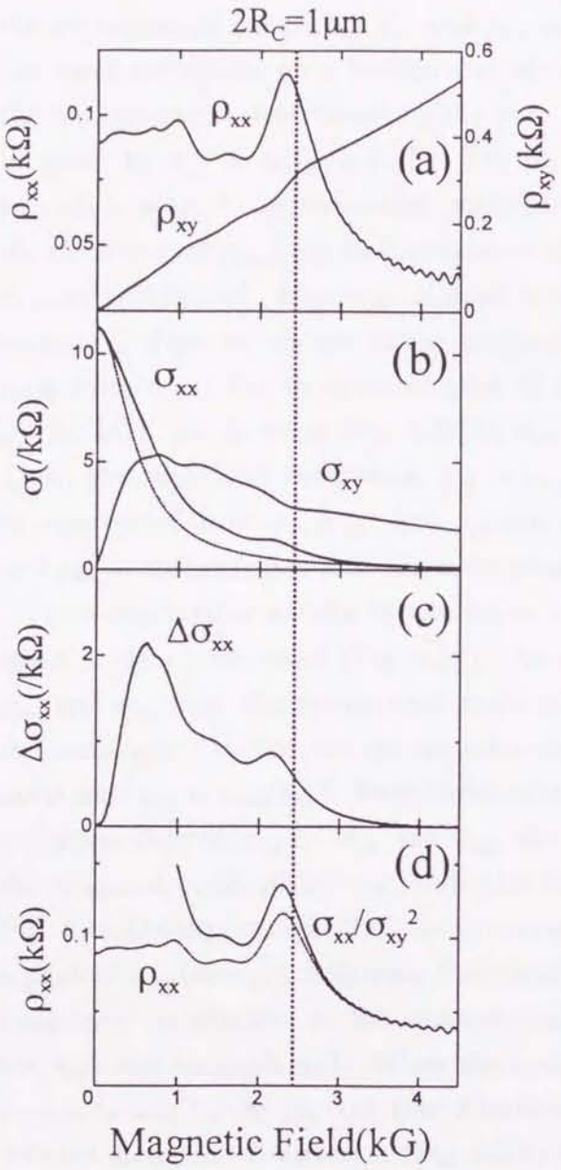

Figure 4.33: (a) Magnetoresistivity ρ_{xx} and Hall resistivity ρ_{xy} in the square antidot lattice ($a = 1$ μm, $d \sim 0.1$ μm). (b) Solid lines show the experimental σ_{xx}, σ_{xy}, and dotted line shows classical magnetoconductivity $\sigma^0_{xx} = \alpha/(1 + \beta B^2)$ where α and β are fitting parameters (α =11.2 and β =432). (c) Different conductivity ($\Delta\sigma_{xx} = \sigma_{xx} - \sigma^0_{xx}$). (d) Resistivity re-constructed from $\sigma_{xx}/\sigma^2_{xy}$ (solid line) and ρ_{xx} (dotted line). A vertical dotted line is drawn at $2R_c = 1$ μm.

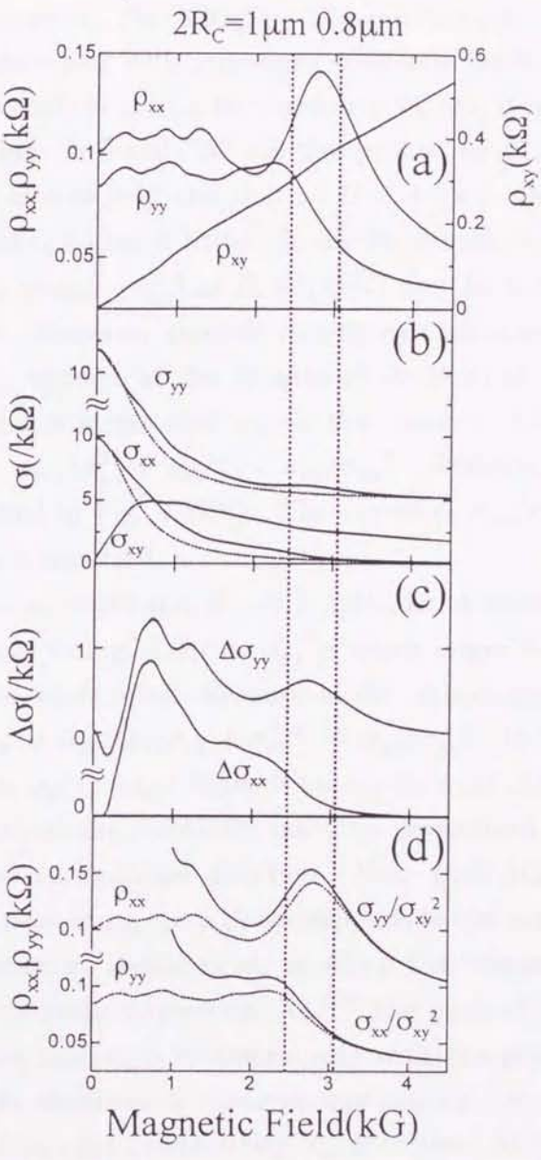

Figure 4.34: (a) Magnetoresistivies ρ_{xx}, ρ_{yy} and Hall resistivity ρ_{xy} in rectangular lattice (1 μm$\times$0.8μm, d$\sim$ 0.1 μm). (b) Solid lines show the experimental σ_{xx}, σ_{yy}, and σ_{xy}, and dotted lines show classical magnetoconductivities σ^0_{xx} and σ^0_{yy}. (c) Different conductivities ($\Delta\sigma_{xx} = \sigma_{xx} - \sigma^0_{xx}$, $\Delta\sigma_{yy} = \sigma_{yy} - \sigma^0_{yy}$). (d) Solid lines are resistivities re-constructed from $\sigma_{yy}/\sigma^2_{xy}$ or $\sigma_{xx}/\sigma^2_{xy}$, and dotted lines are ρ_{xx} or ρ_{xx}. Two vertical dotted lines are drawn at $2R_c = 1$ μm and 0.8 μm.

conductor (see Appendix B). The experimental conductivity σ_{xx} and σ_{xy} converted from the experimental resistivity ρ_{xx} and ρ_{xy} are shown in Fig. 4.33(b). The conductivity σ_{xx} has some structures on a background which decreases with increasing magnetic fields. If the background is determined by the pure classical effect in a homogeneous 2DEG, it may be given by $\sigma^0_{xx} = \alpha/(1+\beta B^2)$. The parameter "$\alpha$" and "$\beta$" are determined by fitting procedure with the experimental conductivity at zero-field and that at $B = 4.5$ kG where the deviation of ρ_{xy} from Hall resistance of 2DEG region is little. To see the structures of σ_{xx}, we subtract σ^0_{xx} from σ_{xx}. A peak of $\Delta\sigma_{xx}$ ($=\sigma_{xx} - \sigma^0_{xx}$) at $B \sim 0.8$ kG may be trivial because it depends on two fitting parameters. However, another structures undoubtedly stem from σ_{xx}. The pronounced peak of $\Delta\sigma_{xx}$ appears at the vicinity of the peak of ρ_{xx} ($\sim$ 2.2 kG). As shown in Fig. 4.33(b), σ_{xy} is much larger than σ_{xx} in the region $\sim$ 2 kG. Thus, the resistivity component ρ_{xx} is $\rho_{xx} = \sigma_{xx}/(\sigma^2_{xx} + {\sigma_{xy}}^2) \sim \sigma_{xx}/{\sigma_{xy}}^2$. Resistivities re-constructed from $\sigma_{xx}/{\sigma_{xy}}^2$ and ρ_{xx} are plotted in Fig. 4.33(d). The curves of $\sigma_{xx}/{\sigma_{xy}}^2$ and ρ_{xx} almost coincide near the main peak as is expected.

In a rectangular antidot lattice ($a_x = 1$ μm, $a_y = 0.8$ μm, $d \sim 0.1$ μm), the anisotropy effect is clearly observed (Fig. 4.34). As shown in Fig. 4.34(b), σ_{xy} is much larger than σ_{xx} and σ_{yy} near the pronounced peaks of the resistivities. Because of the anisotropy of the rectangular lattice, we get the relation $\rho_{xx} = \sigma_{yy}/(\sigma_{xx}\sigma_{yy} + {\sigma_{xy}}^2) \sim \sigma_{yy}/{\sigma_{xy}}^2$. In the same way, ρ_{yy} is $\sigma_{xx}/{\sigma_{xy}}^2$. From these relations, ρ_{xx} (or ρ_{yy}) depends on σ_{yy} (or σ_{xx}). That is, in the case of $\sigma_{xy} \gg \sigma_{xx}$ and σ_{yy}, the peak of the resistivity must be determined by the diagonal conductivity perpendicular to the current flow direction. Near B=3 kG in Fig. 4.34, the magnetic field of the pronounced peak of ρ_{xx} (or ρ_{yy}) corresponds to the one of a peak of σ_{yy} (or σ_{xx}). Following the consideration by Baskin et al., in which the "runaway trajectory" is effective at the commensurability peaks (Appendix A),[120] the peak of σ_{yy} (or σ_{xx}) can be explained. When the cyclotron motion is commensurate with the period perpendicular to the current flow direction, the electrons on the runaway trajectories are diffused along the Y-direction (Fig. 4.35(a)). Thus, the conductivity σ_{yy} increases. At this condition, σ_{xx} is not enhanced. On the other hand, at $2R_c = a_x$ where the electrons are guided along the X-direction (Fig. 4.35(b)), the peak of σ_{xx} appears and the peak of ρ_{yy} is observed. Here, we emphasize that it is important that the electrons are diffused along the antidot arrays perpendicular to the current flow direction. Recently, Nagao has performed a numerical simulation on a rectangular antidot lattice and has showed that anisotropic behavior of the most pronounced peak can be explained by the diffusion of electrons along the antidot array perpendicular to the current when the cyclotron diameter is commensurate with that period.[121] The calculation by Fleischmann *et al.* have showed that the trajectories belonging to a "pinned orbit" are not effective (Appendix A).[119] Their result agrees with our consideration because the electrons on "runaway trajectory" do not stay at an antidot for a long time. However, in the case of $\sigma_{xy} \ll \sigma_{xx}, \sigma_{yy}$, the resistivity ρ_{xx} is proportional to

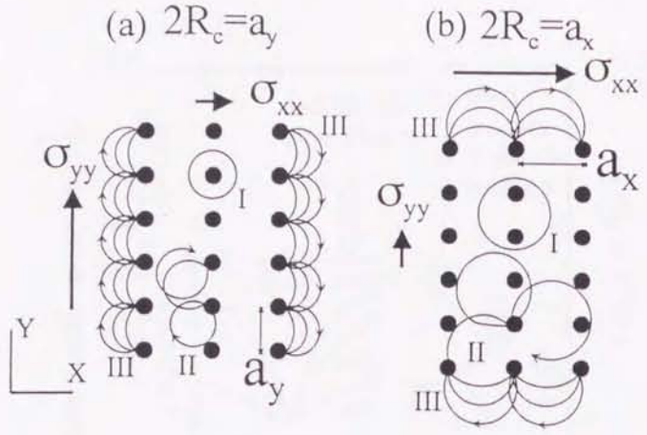

Figure 4.35: Schematic electron trajectories in rectangular lattice. At the $2R_c = a_y$ (a), conductivity σ_{yy} is enhanced. In the same way, at the $2R_c = a_x$ (b), conductivity σ_{xx} is enhanced.

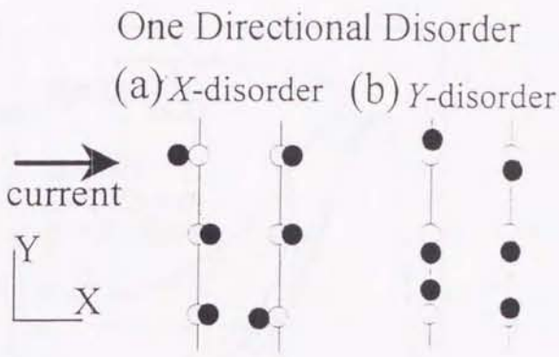

Figure 4.36: Schematic view of one-directional disordered lattices (X- or Y-disorder).

$1/\sigma_{xx}$. At this condition, Schuster *et al.* suggests that the pinned orbits may be dominant at the peaks of the commensurability oscillations.[111]

Our model of the commensurability oscillations can explain the previous experimental results described in previous paragraphs. In rectangular lattices, the peak position is determined only by a_y (Fig. 4.28). When the rectangular lattice is tilted, the peak, which appears at $2R_c$=*shorter period*, decreases with increasing tilted angle (Fig. 4.30), because the contribution of the electron diffusion to σ_{yy} decreases in the tilted antidot arrays. In the one-directionally disordered lattices (Fig. 4.26), the lengths between the antidots along Y-direction vary more with Y-directional disorder than with X-directional disorder, because Y-directional disorder changes these widths more directly (Fig. 4.36). Thus, the peaks in X-disordered systems are larger than those in Y-disordered systems. In the same way, in the triangular lattices, the main peak fields are determined by the nearest neighbor distance in the lattice (Fig. 4.29), because the commensurate condition is determined by the electrons diffusing along the nearest neighbor distance between the antidots.

4.3.3.6 Negative magnetoresistance due to Anderson localization

In the antidot system, the negative magnetoresistances and strongly temperature dependent resistances have been observed in various antidot lattices at low temperature.[114,116,117,127,128] Some of these experiments have been made in the systems produced by focused ion-beam (FIB) techniques. Since the energy of FIB is so high that the damage around the antidots could not be avoided, the antidot diameter is large enough to be comparable to the period. In the narrow structure, the boundary scattering of electrons by the walls becomes prominent. The negative magnetoresistances have been interpreted as an weak localization by the electron-electron scattering, which is extended from the Al'tshuler-

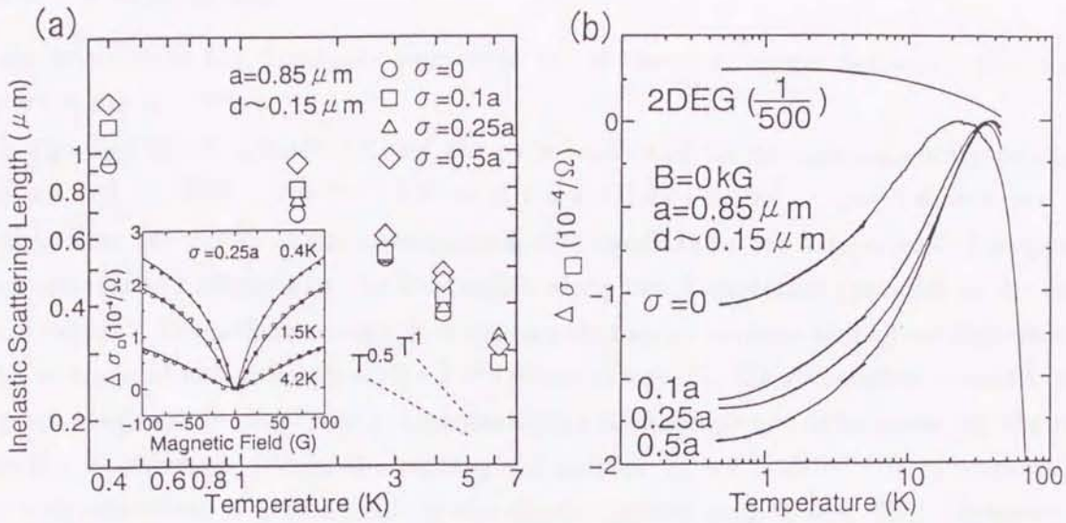

Figure 4.37: (a)Inelastic scattering length in the ordered and the disordered antidot systems. Inset: Magnetoconductance of $\sigma = 0.25a$ in very low magnetic field for differing temperature with the theoretical curves (solid lines). (b)Temperature dependence of the conductance change in the absence of magnetic field.

Aronov[130] and Dugaev-Khmel'nitskii[131] theories in including the specular boundary scattering,[132] and the one-dimensional weak localization by the boundary scattering.[128,129] In other antidot systems,[116,117], the negative magnetoresistance has been explained by a numerical calculation based on a classical model in which the external electric field and Hall field are explicitly taken into account.

The negative magnetoresistance in the very low magnetic field (less than 100 Gauss) is observed both in the ordered and in the disordered antidot system (Fig. 4.37). The negative magnetoresistance is not observed in magnetic field parallel to the plane of the 2DEG. Because of temperature dependence of low field magnetoresistance (shown in Fig. 4.37(a) inset, three symbols) and the disappearance above 10 K, we fit the negative magnetoresistance following the two dimensional weak localization theory of Hikami-Larkin-Nagaoka[133] (Fig. 4.37(a) inset, solid line). The estimated inelastic scattering length from the fitting is about 1 μm at 0.4 K, and decreases with increasing temperature. Since the apparent difference between antidot systems with different σ is not observed, the negative magnetoresistance may be caused by the defects around the antidots.

With decreasing temperature below 20-40 K, the zero field conductance decreases, while, the conductance of the 2DEG (without antidots) region increases (Fig. 4.37(b)). In the two dimensional weak localization theory, the relation between the temperature and the conductance change is expressed as $\Delta\sigma = \alpha_T(e^2/2\pi^2\hbar)lnT$.[134] In our experiments, the value of the coefficient α_T is 3-6. This is much larger than $\alpha_T \sim 1$ which is expected by the conventional week Anderson localization.[134,135] The origin of the temperature dependence in the high temperature region have not yet been revealed.

4.3.4 Conculsion

We investigate the transport properties in the various antidot lattices. The clarified properties are as follows.

In the disordered antidot lattices, the peak heights of the commensurability oscillations decrease with increasing the fluctuations of the antidot location. In an all-directional disordered lattice, the peaks of the commensurability oscillations are suppressed. However, the peaks are scarcely affected by the fluctuation along the X-direction (parallel to the current flow direction). From these results, it is appears that no commensurability oscillations occurs in the absence of the ordering of the Y-direction arrays. In the rectangular antidot lattice, the peak magnetic fields of the commensurability oscillations are determined by the period along the Y-direction. When the rectangular antidot lattice is tilted (tilted angle=θ), the peak magnetic field is determined by the shorter period at $0 \leq \theta < 90°$. However, with increasing θ, the peak height decreases. In the isosceles triangular lattice, the commensurate condition is determined by the nearest neighbor distance between the antidots. The dependence of the commensurability oscillations on the number of antidot arrays (N) and the relationship between the current flow direction and the tilted rectangular antidot cell are investigated. With decreasing N, the peaks of the commensurability oscillations decrease. However, even at N= 1, the peaks do not vanish. In the case of $\sigma_{xy} \gg \sigma_{xx}$ and σ_{yy}, it is found that the fundamental peak on resistivity is determined by the peak on the conductivity perpendicular to the current flow direction. Consequently, we find that the behavior of the conductance perpendicular to the current flow direction determines the oscillations of the resistivity of system. This is the origin of the fundamental peak in the commensurability oscillations.

The negative magnetoresistance in very low magnetic field (less than 100 Gauss) is observed both in the ordered and the disordered antidot lattices due to the two dimensional weak localization effect. Moreover, the large temperature dependence of the conductance, which can not be explained by the conventional localization theory, is observed.

Chapter 5

Summary

In this thesis, several ballistic electron transport properties in GaAs/AlGaAs mesoscopic structures are studied.

- **Study of Magnetic Electron Focusing Effect**
  Magnetic electron focusing effect is investigated by paying attention to its electron density (n_s) dependence in a GaAs/AlGaAs device with multi-parallel-terminal. With increasing n_s, a ballistic elastic scattering length increases, but a specularity at boundary decreases. In a configuration in which a extra probe is located in between emitter and collector probes, electrons entered the extra probe are "reflected", and the focusing peak can be clearly observed. The "extra probe reflection" is revealed as the re-emission of electrons from the piled up extra probe by the experiment of the devices with "byway channel".

- **Investigation of Electron Emission Distribution from oblique wire**
  Electron angular distribution from a oblique wire which is tilted under 45° from vertical direction to 2DEG boundary is investigated. A shift of angular distribution from the oblique wire is not 45° but about 10° from perpendicular direction to the 2DEG. The result shows that the electron distribution depends on the ansymmetry just at the orifice. In the investigation of the magnetic electron focusing effect, both peak positions from oblique and vertical wires are almost same. From the simulation of the focusing effect with a classical billiard model, no experimental peak shift is observed in the magnetic electron focusing effect if the remarkable collimation does not occurs.

- **Transport Property in Lateral Antidot lattice**
  We investigate the commensurability oscillations paying attention to the relationship between the lattice anisotropy and the current flow direction. It is found that the oscillation peaks in rectangular antidot lattices is determined by the order perpendicular to the current flow direction. When the rectangular antidot lattice is tilted (tilted angle=θ), the peak magnetic field is determined by the shorter period of the

cell at $0 \leq \theta < 90°$, while, at $\theta = 90°$, the peak field is determined only by the period perpendicular to the current flow direction. In the isosceles triangular lattice, the field of the pronounced commensurate peak is determined by the nearest neighbor distance between antidots. Moreover, the peaks do not vanish even in the single array perpendicular to the current flow direction. Consequently, we find the that the commensurability oscillations are determined by the conductivity perpendicular to the current flow direction, and peak on the conductivity is explained by the electron diffusion along its period on the runaway trajectory.

Appendix A: Existent models for the commensurability oscillations

In this appendix, we introduce the two models to illustrate the commensurability oscillations in the square antidot lattice. First model has been proposed by Weiss *et al.* Their model stems from the trapped electrons by "pinned orbit".[105] However, there are no reason that the electron can stay near antidot for a long time because the potential of antidot pillars repulses the electrons. This model is not adequate for the electron transport property. But, it is useful to predict the peak magnetic fields. Second model is derived by the classical chaotic dynamics.[119,120] By the numerical calculation in the *cos*-function like soft wall potentials, Fleischmann *et al.* have classified the electron trajectories into two kinds of trajectories: the pinned trajectory and the chaotic trajectory. As the result, they emphasize that the chaotic trajectories is the majority in the contribution to the resistance peaks. From the standing point of dynamics chaos theory, Baskin *et al.* have also calculated the electron trajectories in an antidot lattice with hard wall.[120] They calculate the diffusion coefficient of the lattice, and analyze the association between the coefficient and the resistance peak.

Pinned orbits model

This model is based on the classical electron movement like a pinball in the periodic hard wall pillars.[105] From the fact that the peak magnetic fields of the oscillations correspond to the fields where the classical cyclotron motions encircle some antidots, it appears intuitively that the electrons are trapped by antidots. The model involves three different electron orbits: *pinned*, *scattered* and *drifting* one. Electrons with Fermi energy are divided into three kinds of orbit fraction (f_p, f_s, f_d) in accordance with electron position and moving direction. Since the conductance is assumed to be determined by the fraction of f_s and f_d, the resistance

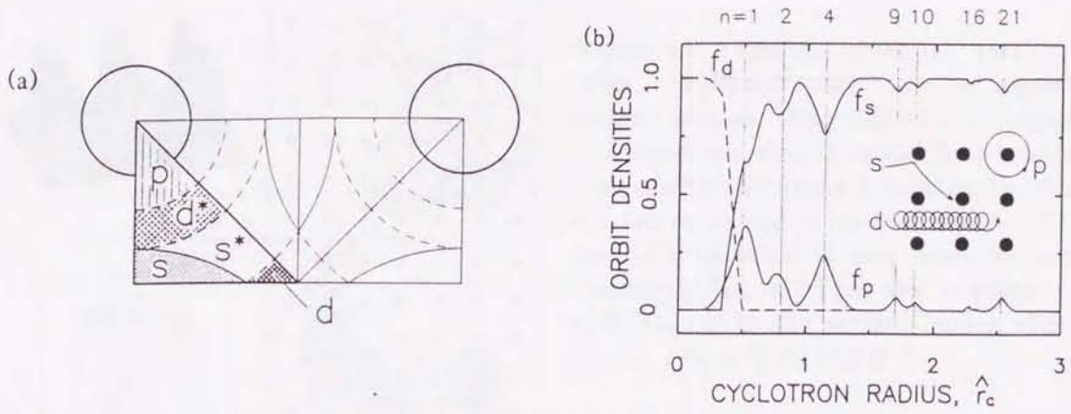

Figure 5.1: (a) Real space diagram which is divided into three zone: *pinned*, *scattered* or *drifting* orbit. Electrons are divided into three kinds of orbit fraction (f_p, f_s, f_d) in accordance with electron position and moving direction (b). (From Ref.105.)

peak appear at the field where f_p increases.

This model can be successively applied to square lattice and triangle lattice.[105,106] However, in an antidot lattice with anisotropic cell; e.g., a rectangular cell, the peak magnetic fields depend on the current flow direction.[107-110] This anisotropy could not be explained by the pinned electron orbit model because the electrons should be trapped around the antidots irrespective of the current flow direction in the pinned electron model.

Weiss also has suggested that the validity of the pinball model becomes questionable for large d/a, and the electron dynamics in a "soft" antidot potential can not be described in terms of conventional circular cyclotron motion ($2R_c = 2\hbar k_F/eB$).

Chaotic Orbits Model

Fleischmann *et al.*[119] applied a periodic potential system to Kubo-type linear response system.[18] They have solved the classical Hamiltonian of electron motion

$$H = \frac{1}{2m}(\vec{p} - e\vec{A})^2 + U(x,y) \tag{5.1}$$

under a model potential

$$U(x,y) = U_0\,[\cos(2\pi x)\cos(2\pi y)]^\gamma \tag{5.2}$$

where $\vec{p}$ is the electron momentum and $\vec{A}$ the vector potential. The parameter γ control the steepness of antidot wall. Trajectories $x(t)$, $y(t)$, and corresponding velocities $v_x(t) = \dot{x}$, $v_y(t) = \dot{y}$ are obtained in the numerical results. The phase space is generally divided into two regions: regular cyclotron like motion and chaotic motion. Figure 5.2 shows the poincaré surface of section (y,v_y) at $x = 0$. The electrons belonging to the island behave as regular motion around the antidot, that is, behave as the pinned electrons in the Weiss's model.

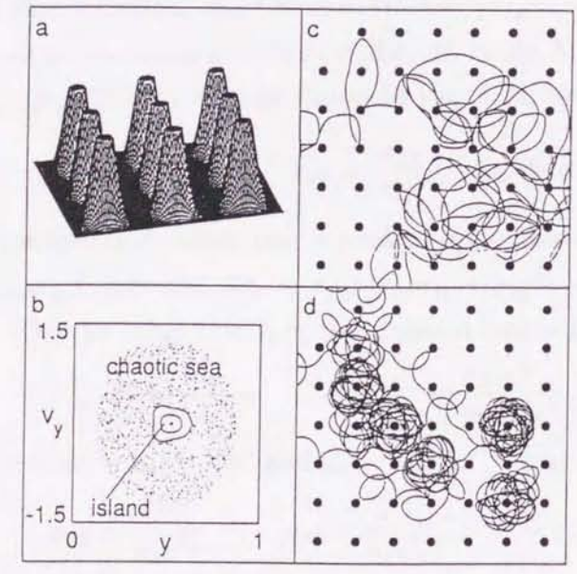

Figure 5.2: (a)Model potential (γ=4) of antidot. (b)Phase space map for regular or chaotic motion. The electrons belonging to the island stay around antidot for a long time, whereas the electrons belonging to chaotic sea travel around in antidot lattice. Examples of trajectories in real space for incommensurate ($R_c = a$) (c) and commensurate ($2R_c$=a) (d) in the antidot lattice with period a. (From Ref.119,108.)

These electrons do not contribute to the conductance. In accordance with velocity correlation $\langle \tilde{v}_i(t)\tilde{v}_j(0)\rangle$ in the Kubo-type formula, the conductivity σ_{ij} can be expressed as

$$\sigma_{ij} \propto \int_0^\infty e^{(-t/\tau)} \langle \tilde{v}_i(t)\tilde{v}_j(0)\rangle \, dt. \tag{5.3}$$

Because only chaotic trajectories contribute to the conductivity, the integral is taken only over chaotic trajectories. These numerical results are in good agreement with experiments in the square antidot lattice. Consequently, Fleischmann *et al.* conclude that the magnetoresistance peaks mainly are not caused by the varying number of pinned (regular) orbit, but by correlations within the chaotic region.

On the other hand, Baskin *et al.*[120] have calculated the electron trajectories in an antidot lattice with hard wall from the standing point of dynamic chaos theory. They find that the diffusion coefficient (D_{xx}) of the lattice is enhanced at $2R_c = a$ by the contribution of the "runaway trajectories" (trajectory II in Fig.4.32). They argue that the oscillation peaks of D_{xx} coincide the peaks of measured resistance in the antidot lattice.

Appendix B: Conductivity and resistivity tensor

In the two-dimensional case, the relation between the external electric field ($\vec{E}$) and the current density ($\vec{J}$) in the magnetic field are

$$\begin{bmatrix} J_x \\ J_y \end{bmatrix} = \begin{bmatrix} \sigma_{xx} & \sigma_{xy} \\ \sigma_{yx} & \sigma_{yy} \end{bmatrix} \begin{bmatrix} E_x \\ E_y \end{bmatrix} \quad , \quad \begin{bmatrix} E_x \\ E_y \end{bmatrix} = \begin{bmatrix} \rho_{xx} & \rho_{xy} \\ \rho_{yx} & \rho_{yy} \end{bmatrix} \begin{bmatrix} J_x \\ J_y \end{bmatrix} \quad . \tag{5.4}$$

At $J_y = 0$ ($J_x \neq 0$), J_x and ρ_{xx} in the anisotropic lattice are expressed as :

$$J_x = \sigma_{xx}(1 + \frac{\sigma_{xy}^2}{\sigma_{xx}\sigma_{yy}})E_x \quad , \quad \rho_{xx} = \frac{\sigma_{yy}}{\sigma_{xx}\sigma_{yy} + \sigma_{xy}^2} \quad . \tag{5.5}$$

In this equation, the *Onsager relation* ($\sigma_{xy} = -\sigma_{yx}$) and $E_y = (\sigma_{xy}/\sigma_{yy})E_x$ are used. At the peak of commensurability oscillations in the higher magnetic fields, σ_{xy} is larger than σ_{xx} or σ_{yy} ($\sigma_{xy} \gg \sigma_{xx},\ \sigma_{yy}$) as shown in Fig. 4.33; we approximate J_x and ρ_{xx} as

$$J_x \simeq \frac{{\sigma_{xy}}^2}{\sigma_{yy}} E_x \quad , \quad \rho_{xx} \simeq \frac{\sigma_{yy}}{{\sigma_{xy}}^2} \quad (\sigma_{xy} \gg \sigma_{xx},\ \sigma_{yy}) \quad . \tag{5.6}$$

This equations show that a peak of σ_{yy} makes a peak on ρ_{xx}. At low magnetic fields ($\sigma_{xy} \ll \sigma_{xx}, \sigma_{yy}$), however, $\rho_{xx} = \sigma_{yy}/(\sigma_{xx}\sigma_{yy} + {\sigma_{xy}}^2) \sim 1/\sigma_{xx}$ approximately.

On the other hand, in the classical Drude model, σ_{xx}^0 and σ_{xy}^0 are

$$\sigma_{xx}^0 = \frac{\sigma_0}{1 + {\omega_c}^2\tau^2} \quad , \quad \sigma_{xy}^0 = -\frac{\sigma_0\omega_c\tau}{1 + {\omega_c}^2\tau^2} \tag{5.7}$$

where $\sigma_0 = n_s e^2\tau/m^*$ and $\omega_c = eB/m^*$. Then, ρ_{xx} and ρ_{xy} are

$$\rho_{xx} = \frac{m}{n_s e^2 \tau} \quad , \quad \rho_{xy} = \frac{1}{n_s e} B \quad . \tag{5.8}$$

The resistance ρ_{xx} is independent on the magnetic field (B), and ρ_{xy} is proportional with B.

Symbols and Shortened signs

symbol,sign	means
2DEG	Two dimensional electron gas
a	Period of antidot lattice
d	Diameter of antidot
B	Magnetic Field
B_{foc}	Peak Magnetic Field in Magnetic focusing effect ($= 2\hbar k_{\mathrm{F}}/e\Delta L$)
e	Single electron charge
$\vec{E}$	Electric field
EB	Electron beam lithography
E_{F}	Fermi energy ($= (\hbar k_{\mathrm{F}})^2/2m^*$)
f	Fermi distribution function
h	Plank's constant ($= 2\pi\hbar$)
HEMT	GaAs/AlGaAs heterostructure with high mobility two-dimensional electron gas (grown by MBE)
k_{F}	Fermi wave vector ($= (2\pi n_{\mathrm{s}})^{1/2}$)
I_{B}	Byway current
l_{e}	Elastic mean free path of electron derived from μ and n_{s}
l_{b}	Ballistic elastic mean free path of electron
LED	Light emitting diode (GaAs, $\lambda \sim$950 nm)
m^*	Effective mass in GaAs ($= 0.067m_{\mathrm{e}}$)
n_{s}	Carrier density of 2DEG
p	Specular coefficient (=specularity) of 2DEG boundary
R_{B}	Byway resistance
R_{c}	Semiclassical cyclotron radius ($= \hbar k_{\mathrm{F}}/eB$)
PMMA	Organic resist material for EB (=PolyMetylMethacrylate)
SdH oscillations	Shubnikov-de Haas oscillations
v_{F}	Fermi velocity ($= \hbar k_{\mathrm{F}}/m^*$)
σ	Standard deviation in Gaussian distribution
$\sigma_{\square}$	Seat conductance
$\sigma_{xx}, \sigma_{yy}, \sigma_{xy}$	Conductivity tensor
$\rho_{xx}, \rho_{yy}, \rho_{xy}$	Resistivity tensor
μ	Hall mobility
ω_{c}	Cyclotron frequency ($= eB/m^*$)
ΔL	Separation length between emitter and collector
τ	Scattering time of electron

References

[1] R. Landauer, IBM J. Res. Dev. **1**, 223 (1957).

[2] M. Büttiker, Y. Imry, R. Landauer, and S. Pinhas, Phys. Rev. B **31**, 6207 (1985).

[3] M. Büttiker, Phys. Rev. Lett. **57**, 1761 (1986).

[4] M. Büttiker, IBM J. Res. Develop. **32**, 317 (1988).

[5] see, e.g., D. P. Kern, in *Low-Dimensional Electronics Systems*, edited by G. Bauer, F. Kuchar, and H. Heinrich (Springer-Verlag, Belrin, 1992).

[6] B. L. Al'tshuler, A. G. Aronov, and B. Z. Spivak, Pis'ma Zh. Eksp. Teor. Fiz. **33**, 101 (1981) [JETP Lett.**33**, 94 (1981)].

[7] D. Y. Sharvin and Y. V. Sharvin, Pis'ma Zh. Eksp. Teor. Fiz. **34**, 285 (1981) [JETP Lett.**34**, 272 (1981)].

[8] C. P. Umbach, S. Washburn, R. B. Laibowitz, and R. A. Webb, Phys. Rev. B **50**, 4048 (1984).

[9] A. D. Stone, Phys. Rev. Lett. **54**, 2692 (1985).

[10] Y. Aharanov and D. Bohm, Phys. Rev. **115**, 485 (1959).

[11] R. A. Webb, S. Washburn, C. P. Umbach, and R. B. Laibowitz, Phys. Rev. Lett. **54**, 2696 (1985).

[12] B. J. van Wees, H. van Houten, C. W. J. Beenakker, J. G. Williamson, L. P. Kouwenhoven, D. van der Marel, and C. T. Foxon, Phys. Rev. Lett. **60**, 848 (1988).

[13] D. A. Wharam, T. J. Thornton, R. Newbury, M. Pepper, H. Ahmed, J. E. F. Frost, D. G. Hasko, D. C. Peacok, D. A. Ritchie, and G. A. C. Jones, J. Phys. C **21**, L209 (1988).

[14] U. Meirav, M. A. Kastner, and S. J. Wind, Phys. Rev. Lett. **65**, 771 (1990).

[15] L. Onsager, Phys. Rev. **37**, 405 (1931).

[16] H. B. G. Casimir, Rev. Mod. Phys. **17**, 343 (1945).

[17] L. D. Landau, Zh. Exp. Teor. Fiz. **30**, 1058 (1956) [Soviet Phys. JETP **3**, 920 (1957)].

[18] R. Kubo, J. Phys. Soc. Jpn. **12**, 570 (1957).

[19] P. W. Anderson, Phys. Rev. **109**, 1492 (1958).

[20] Y. V. Sharvin, Zh. Eksp. Teor. Fiz. **48**, 984 (1965) [Sov. Phys. JETP **21**, 655 (1965)].

[21] L. Esaki and R. Tsu, IBM Research Note RC-2418. (1969).

[22] V. S. Tsoi, ZhETF Pis. Red. **19**, 114 (1974) [JETP Lett. **19**, 70 (1974)].

[23] R. Dingle, H. L. Stŕmer, A. C. Gossard, and W. Wiegmann, Appl. Phys. Lett. **33**, 665 (1978).

[24] E. Abrahams, P. W. Anderson, D. C. Licciardello, and T. V. Ramakrishnan, Phys. Rev. Lett. **42**, 673 (1979).

[25] T. Miura, S. Hiyamizu, T. Fujii, and K. Nanbu, Jpn. J. Appl. Phys. **19**, L225 (1980).

[26] K. von Klitzing, and G. Dorda, and M. Pepper, Phys. Rev. Lett. **45**, 494 (1980).

[27] D. C. Tsui, H. L. Stormer, and A. C. Gossard, Phys. Rev. Lett. **48**, 1559 (1982).

[28] R. B. Laughlin, Phys. Rev. Lett. **50**, 394 (1983).

[29] M. L. Roukes, A. Scherer, S. J. Allen, Jr., H. G. Craighead, R. M. Ruthen, E. D. Beebe, and J. P. Harbison, Phys. Rev. Lett. **59**, 3011 (1987).

[30] Y. Takagaki, K. Gamo, S. Namba, S. Ishida, S. Takaoka, K. Murase, K. Ishibashi, and Y. Aoyagi, Solid State Commun. **68**, 1051 (1988).

[31] J. K. Jain, Phys. Rev. Lett. **63**, 199 (1989).

[32] H. W. Jiang, H. L. Stormer, D. C. Tsui, L. N. Pfeiffer, and K. W. West, Phys. Rev. B **40**, 12013 (1989).

[33] R. L. Willet, M. A. Paalanen, R. R. Ruel, K. W. West, L. N. Pfeiffer, and D. J. Bishop, Phys. Rev. Lett. **65**, 112 (1990).

[34] D. Weiss, K. von Klitzing, K. Ploog, and G. Weimann, Europhys. Lett. **8**, 179 (1989).

[35] E. S. Alves, P. H. Beton, M. Henini, L. Eaves, P. C. Main, O. H. Hughes, G. A. Toombs, S. P. Beaumont, and C. D. W. Wilinson, J. Phys. C **1**, 8257 (1989).

[36] C. M. Marcus, A. J. Rimberg, R. M. Westervelt, P. F. Hopkins, and A. G. Gossard, Phys. Rev. Lett. **69**, 506 (1992).

[37] see for exsample, J. M. Ziman, *Principles of the Theory of Solids*, "chapter 7" (Cambridge University Press).

[38] A. D. Stone and A. Szafer, IBM J. Res. Develop. **32**, 384 (1988).

[39] A. Kawabata, J. Phys. Soc. Jpn. **58**, 372 (1989).

[40] A. Y. Cho and J. R. Arthur, Jr., *Progress in Solid State Chemistry*, edited by G. Somerjai and J. McCaldin (Pergamon, New York, 1975), Vol.10, p157.

[41] S. Hiyamizu, J. Saito, K. Nanbu, and T. Ishikawa, Jpn. J. Appl. Phys. **22**, L609 (1983).

[42] L. Pfeiffer, K. W. West, H. L. Stomer, and K. W. Baldwin, Appl. Phys. Lett. **55**, 1888 (1989).

[43] T. Saku, Y. Hiraayama, and Y. Horikoshi, Jpn. J. Appl. Phys. **30**, 902 (1991).

[44] T. Miura, K. Joshin, S. Hiyamizu, K. Hikosaka, and M. abe, Jpn. J. Appl. Phys. **20**, L598 (1981).

[45] D. C. Tsui, A. C. Gossard, G. Kaminski, and W. Wiegmann, Appl. Phys. Lett. **39**, 712 (1981).

[46] T. Ando, J. Phys. Soc. Jpn. **51**, 3900 (1982).

[47] W. Walukiewicz, H. E. Ruda, J. Lagowski, and H. C. Gatos, Phys. Rev. B **30**, 4571 (1984).

[48] K. Hirakawa and H. Sakaki, Phys. Rev. B **33**, 8291 (1986).

[49] P. M. Mooney, J. Appl. Phys. **67**, R1 (1990).

[50] Y. Yuba, T. Ishida, K. Gamo, and S. Namba, J. Vac. Sci. Technol. B **6**, 253 (1988).

[51] H. F. Wong, D. L. Green, T. Y. Liu, D. G. Lishan, M. Bellis, E. L. Hu, P. M. Petroff, P. O. Holtz, and J. L. Merz, J. Vac. Sci. Technol. B **6**, 1906 (1988).

[52] M. Yamazawa, T. Matsumoto, H. Tanigushi, T. Sakamoto, Y. Takagaki, Y. Yuba, S. Takaoka, K. Gamo, K. Murase, and S. Namba, Jpn. J. Appl. Phys. **30**, 3261 (1991).

[53] J. Lindhard, M. Scharff, and H. Schiott, K. Dan. Vidensk. Selsk. Mat. Fys. Medd. **33**, 14 (1963).

[54] J. P. Biersack and L. G. Haggmark, Nucl. Instrum. Methods **174**, 189 (1980).

[55] J. F. Ziegler, J. P. Biersack, and U. Litimark, *The Stopping and Range of Ions on Solids*, (Pergamon, New York, 1985).

[56] A. F. Burenkov, F. F. Komarov, M. A. Kumakhov, and M. M. Temkin, *Tables of Ion Implantation Spatial Distributions* (Gordon and Breach, New York, 1986).

[57] N. G. Stoffel, J. Vac. Sci. Technol. B **10**, 651 (1992).

[58] J. Spector, H. L. Stormer, K. W. Baldwin, L. N. Pfeiffer, and K. W. West Appl. Phys. Lett. **56**, 1290 (1990).

[59] U. Sivan, M. Heiblum, C. P. Umback, and H. Shrikman, Phys. Rev. Lett. **41**, 7937 (1990).

[60] J. Spector, J. S. Weiner, H. L. Stormer, K. W. Baldwin, L. N. Pfeiffer, and K. W. West Surface Science **263**, 240 (1992).

[61] V. S. Tsoi and I. I. Razgonov, Pis'ma Zh. Eksp. Teor. Fiz. **25**, 30 (1977) [JETP Lett. **25**, 26 (1977)].

[62] V. S. Tsoi, J. Bass, P. A. M. Benistant, H. van Kempen, E. L. M. Payens, and P. Wyder, J. Phys. F. **9**, L221 (1979).

[63] C. W. J. Beenakker, H. van Houten, and B. J. van Wees, Europhys. Lett. **7**, 359 (1988).

[64] H. van Houten, B. J. van Wees, J. E. Mooij, C. W. J. Beenakker, J. G. Williamson, and C. T. Foxon, Europhys. Lett. **5**, 721 (1988).

[65] H. van Houten, C. W. J. Beenakker, J. G. Williamson, M. E. I. Broekaart, P. H. M. van Loosdrecht, B. J. van Wees, J. E. Mooij, C. T. Foxon, and J. J. Harris, Phys. Rev. B **39**, 8556 (1989).

[66] J. Spector, H. L. Stormer, K. W. Baldwin, L. N. Pfeiffer, and K. W. West, Surf. Sci. **228**, 283 (1990).

[67] J. Spector, H. L. Stormer, K. W. Baldwin, L. N. Pfeiffer, and K. W. West Appl. Phys. Lett. **56**, 967 (1990).

[68] A. C. Churchill, G. H. Kim, M. Y. Simmons, D. A. Ritchie, and G. A. C. Jones, Phys. Rev. B **50**, 17636 (1994).

[69] K. Nakamura, D. C. Tsui, F. Nihey, H. Toyoshima, and T. Itoh, Appl. Phys. Lett. **56**, 385 (1990).

[70] F. Nihey, K. Nakamura, M. Kuzuhara, N. Samato, and T. Itoh, Appl. Phys. Lett. **57**, 1218 (1990).

[71] T. Sakamoto, Y. Takagaki, S. Takaoka, K. Gamo, K. Murase, and S. Namba, Jpn. J. Appl. Phys. **30**, L1186 (1991).

[72] K. Nakazato, R. I. Hornsey, R. J. Blaikie, J. R. A. Cleaver, H. Ahmed, and T. J. Thornton, Appl. Phys. Lett. **60**, 1093 (1992).

[73] F. Wakaya, Y. Takagaki, S. Takaoka, K. Murase, Y. Yuba, K. Gamo, and S. Namba, Superlatt. Microstruct. **11**, 273 (1992).

[74] K. Tsukagoshi, S. Takaoka, K. Murase, K. Gamo, and S. Namba, Appl. Phys. Lett. **62**, 1609 (1993).

[75] S. Takaoka, K. Tsukagoshi, S. Wakayama, K. Murase, K. Gamo, and S. Namba, Solid State Commun. **83**, 775 (1992).

[76] J. Spector, H. L. Stormer, K. W. Baldwin, L. N. Pfeiffer, and K. W. West Appl. Phys. Lett. **56**, 2433 (1990).

[77] Y. Hirayama, T. Saku, S.Tarucha, and Y. Horikoshi, Appl. Phys. Lett. **58**, 2672 (1991).

[78] S. Takaoka, S. Wakayama, S. G. Inoue, K. Tsukagoshi, K. Oto, K. Murase, and K. Gamo, Phys. Rev. B **50**, 11661 (1994).

[79] S. G. Inoue, S. Takaoka, K. Tsukagoshi, K. Oto, S. Wakayama, K. Murase, and K. Gamo, to appear in Jpn. J. Appl. Phys.

[80] L. W. Molenkamp, A. A. M. Staring, C. W. J. Beenakker, R. Eppenga, C. E. Timmering, J. G. Williamson, C. J. P. M. Harmans, and C. T. Foxon, Phys. Rev. B **41**, 1274 (1990).

[81] M. Okada, M. Saito, M. Takatsu, K. Kosemura, T. Nagata, H. Ishiwari, and N. Yokoyama, Superlatt. Microstruct. **10**, 493 (1991).

[82] K. L. Shepard, M. L. Roukes, and B. P. van der Gaag, Phys. Rev. Lett. **68**, 2660 (1992).

[83] K. L. Shepard, M. L. Roukes, and B. P. van der Gaag, Phys. Rev. B **46**, 9648 (1992).

[84] D. R. S. Cumming, H. Ahmed, and T. J. Thornton, Appl. Phys. Lett. **60**, 2755 (1992).

[85] Y. Oowaki, J. E. F. Frost, L. Martin-Moreno, M. Pepper, D. A. Ritchie, and G. A. C. Jones Phys. Rev. B **47**, 4088 (1993).

[86] S. Wakayama, K. Tsukagoshi, K. Oto, S. Takaoka, K. Murase, and K. Gamo, Solid State Commun. **92**, 413 (1994).

[87] C. J. B. Ford, T. J. Thornton, R. Newbury, M. Pepper, H. Ahmed, D. C. Peacock, D. A. Ritchie, J. E. F. Frost, and G. A. C. Jones, Phys. Rev. B **38**, 8518 (1988).

[88] C. J. B. Ford, S. Washburn, M. Büttiker, C. M. Knoedler, and J. M. Hong, Phys. Rev. Lett. **62**, 2724 (1989).

[89] M. L. Roukes, A. Scherer, and B. P. Van der Gaag, Phys. Rev. Lett. **64**, 1154 (1990).

[90] Y. Hirayama, S.Tarucha, T. Saku, and Y. Horikoshi, Phys. Rev. B **44**, 3440 (1991).

[91] H. U. Baranger and A. D. Stone, Phys. Rev. Lett. **63**, 414 (1989).

[92] H. U. Baranger, D. P. DiVincenzo, R. A. Jalabert, and A. D. Stone, Phys. Rev. B **44**, 10637 (1991).

[93] C. W. J. Beenakker, and H. van Houten, Phy. Rev. Lett. **63**, 1857 (1989).

[94] R. J. Blaikie, K. Nakazato, J. R. A. Cleaver, and H. Ahmed, Phys. Rev. B **46**, 9796 (1992).

[95] T. Usuki, M. Takatsu, R. A. Kiehl, and N. Yokoyama, Phys. Rev. B **50**, 7615 (1994).

[96] C. W. J. Beenakker, and H. van Houten, Phys. Rev. B **39**, 10445 (1989).

[97] K. Kawamura, T. Ueta, H. Sawano, Jpn. J. Appl. Phys. **31**, 317 (1992).

[98] T. Ando, Phys. Rev. B **44**, 8017 (1991).

[99] J. A. Nixon and J. H. Davies, Phys. Rev. B **41**, 7929 (1990).

[100] J. A. Nixon, J. H. Davies, and H. U. Baranger, Phys. Rev. B **43**, 12638 (1991).

[101] G. M. Gusev, Z. D. Kvon, L. V. Litvin, Yu. V. Nastaushev, A. K. Kalagin, and A. I. Toropov, Pis'ma Zh. Eksp. Teor. Fiz. **55**, 129 (1991) [JETP Lett. **55**, 123 (1992)].

[102] F. Nihey and K. Nakamura, Physica B **184**, 398 (1993).

[103] R. Schuster, K. Ensslin, D. Wharam, S. Kühn, J. P. Kotthaus, G. Böhm, W. Klein, G. Tränkle, and G. Weimann, Phys. Rev. B **49**, 8510 (1994).

[104] F. Nihey, S. W. Hwang, and K. Nakamura, Phys. Rev. B **51**, 4649 (1995).

[105] D. Weiss, M. L. Roukes, A. Menschig, P. Grambow, K. von Klitzing, and G. Weimann, Phys. Rev. Lett. **66**, 2790 (1991).

[106] J. Takahara, T. Kakuta, T. Yamashiro, Y. Takagaki, T. Shiokawa, K. Gamo, S. Namba, S. Takaoka and K. Murase, Jpn. J. Appl. Phys. **30**, 3250 (1991).

[107] R. Schuster, K. Ensslin, J. P. Kotthaus, M. Holland, and C. Stanley, Phys. Rev. B **47**, 6843 (1993).

[108] D. Weiss, K. Richter, E. Vasiliadou, and G. Lütjering, Surf. Sci. **305**, 408 (1994).

[109] R. Schuster and K. Ensslin, Festkörperprobleme (to be published).

[110] K. Tsukagoshi, S. Wakayama, K. Oto, S. Takaoka, K. Murase, and K. Gamo, Superlatt. and Microstruct. **16**, 295 (1994).

[111] R. Schuster, G. Ernst, K. Ensslin, M. Entin, M. Holland, G. Böhm, and W. Klein Phys. Rev. B **50**, 8090 (1994).

[112] K. Tsukagoshi, S. Wakayama, K. Oto, S. Takaoka, K. Murase, and K. Gamo, to appear in Phys. Rev. B.

[113] K. Tsukagoshi, M. Haraguchi, K. Oto, S. Takaoka, K. Murase, and K. Gamo, to appear in Jpn. J. Appl. Phys.

[114] G. M. Gusev, P. Basmaji, Z. D. Kvon, L. V. Litvin, Yu. V. Nastaushev, and A. I. Toropov, J. Phys. Condens. Matter **6**, 73 (1994).

[115] A. Lorke, J. P. Kotthaus, and K. Ploog, Phys. Rev. B **44**, 3447 (1991).

[116] G. Berthold, J. Smoliner, V. Rosskopf, E. Gornik, G. Böhm, and G. Weimann, Phys. Rev. B **45**, 11350 (1992).

[117] G. Berthold, J. Smoliner, V. Rosskopf, E. Gornik, G. Böhm, and G. Weimann, Phys. Rev. B **47**, 10383 (1993).

[118] G. M. Gusev, P. Basmaji, and D. I. Lubyshev, . D. Kvon, L. V. Litvin, Yu. V. Nastaushev, Phys. Rev. B **47**, 9928 (1993).

[119] R. Fleischmann, T. Gaisel, and R. Ketzmerick, Phys. Rev. Lett. **68**, 1367 (1992).

[120] E. M. Baskin, G. M. Gusev, Z. D. Kvon, A. G. Pogosov, and M. V. Entin, Pis'ma Zh. Eksp. Teor. Fiz. **55**, 649 (1991) [JETP Lett. **55**, 678 (1992)].

[121] T. Nagao, submitted to J. Phys. Soc. Jpn.

[122] K. Ensslin and P. M. Petroff, Phys. Rev. B **41**, 12307 (1990).

[123] R. Fleischmann, T. Gaisel, and R. Ketzmerick, Europhys. Lett. **25**, 219 (1994).

[124] H. Xu, Phys. Rev. B **50**, 12254 (1994).

[125] H. Silberbauer and U. Rössler, Phys. Rev. B **50**, 11911 (1994).

[126] I. V. Zouzulenko, F. A. Maao, and E. H. Hauge, Phys. Rev. B **51**, 7058 (1995).

[127] G. M. Sundaram, N. J. Bassom, R. J. Nicholas, G. J. Rees, P. J. Heard, P. D. Prewett, J. E. F. Frost, G. A. C. Jones, D. C. Peacock, and D. A. Ritchie, Phys. Rev. B **47**, 7348 (1993).

[128] Y. Chen, R. J. Nicholas, G. M. Sundaram, P. J. Heard, P. D. Prewett, J. E. F. Frost, G. A. C. Jones, D. C. Peacock, and D. A. Ritchie, Phys. Rev. B **47**, 7358 (1993).

[129] C. T. Liang, C. G. Smith, J. T. Nicholls, R. J. F. Hughes, M. Pepper, J. E. F. Frost, D. A. Ritchie, M. P. Grimshaw, and G. A. C. Jones, Phys. Rev. B **49**, 8518 (1994).

[130] B. L. Al'tshuler and A. G. Aronov, Pis'ma Zh. Eksp. Teor. Fiz. **33**, 515 (1981) [JETP Lett. **33**, 499 (1981)].

[131] V. K. Dugaev and D. E. Khmel'nitskii, Zh. Eksp. Teor. Fiz. **86**, 1784 (1984) [Sov. Phys. JETP **59**, 1038 (1984)].

[132] C. W. J. Beenakker and H. van Houten, Phys. Rev. B **38**, 3232 (1988).

[133] S. Hikami, A. I. Larkin, and Y. Nagaoka, Prog. Theor. Phys. **63**, 707 (1980).

[134] D. J. Bishop, D. C. Tsui, and R. C. Dynes, Phys. Rev. Lett. **44**, 1153 (1980).

[135] T. Ando, A. B. Fowler, and F. Stern, Rev. Mod. Phys. **54**, 437 (1982).